Available online at www.sciencedirect.com

ScienceDirect

Geochimica et Cosmochimica Acta 165 (2015) 44–61

Geochimica et Cosmochimica Acta

www.elsevier.com/locate/gca

Fractionation of Fe isotopes during Fe(II) oxidation by a marine photoferrotroph is controlled by the formation of organic Fe-complexes and colloidal Fe fractions

Elizabeth D. Swanner [a,*,1], Wenfang Wu [a,b,1], Ronny Schoenberg [a], James Byrne [a], F. Marc Michel [c], Yongxin Pan [b], Andreas Kappler [a]

[a] *Department of Geosciences, University of Tübingen, Tübingen, Germany*
[b] *Key Laboratory of Earth and Planetary Physics, Institute of Geology and Geophysics, Chinese Academy of Sciences, Beijing, China*
[c] *Department of Geosciences, Virginia Tech, Blacksburg, VA, USA*

Received 18 August 2014; accepted in revised form 10 May 2015;

Abstract

Much interest exists in finding mineralogical, organic, morphological, or isotopic biosignatures for Fe(II)-oxidizing bacteria (FeOB) that are retained in Fe-rich sediments, which could indicate the activity of these organisms in Fe-rich seawater, more common in the Precambrian Era. To date, the effort to establish a clear Fe isotopic signature in Fe minerals produced by Fe(II)-oxidizing metabolisms has been thwarted by the large kinetic fractionation incurred as freshly oxidized aqueous Fe(III) rapidly precipitates as Fe(III) (oxyhydr)oxide minerals at near neutral pH. The Fe(III) (oxyhydr)oxide minerals resulting from abiotic Fe(II) oxidation are isotopically heavy compared to the Fe(II) precursor and are not clearly distinguishable from minerals formed by FeOB isotopically. However, in marine hydrothermal systems and Fe(II)-rich springs the minerals formed are often isotopically lighter than expected considering the fraction of Fe(II) that has been oxidized and experimentally-determined fractionation factors. We measured the Fe isotopic composition of aqueous Fe (Fe_{aq}) and the final Fe mineral (Fe_{ppt}) produced in batch experiment using the marine Fe(II)-oxidizing phototroph *Rhodovulum iodosum*. The $\delta^{56}Fe_{aq}$ data are best described by a kinetic fractionation model, while the evolution of $\delta^{56}Fe_{ppt}$ appears to be controlled by a separate fractionation process. We propose that soluble Fe(III), and Fe(II) and Fe(III) extracted from the Fe_{ppt} may act as intermediates between Fe(II) oxidation and Fe(III) precipitation. Based on ^{57}Fe Mössbauer spectroscopy, extended X-ray absorption fine structure (EXAFS) spectroscopy, and X-ray total scattering, we suggests these Fe phases, collectively $Fe(II/III)_{interm}$, may consist of organic-ligand bound, sorbed, and/or colloidal Fe(II) and Fe(III) mineral phases that are isotopically lighter than the final Fe(III) mineral product. Similar intermediate phases, formed in response to organic carbon produced by FeOB and inorganic ligands (e.g., SiO_4^{4-} or PO_4^{3-}), may form in many natural Fe(II)-oxidizing environments. We propose that the formation of these intermediates is likely to occur in organic-rich systems, and thus may have controlled the ultimate isotopic composition of Fe minerals in systems where Fe(II) was being oxidized by or in the presence of microbes in Earth's past.

Abbreviations: FeOB, Fe(II)-oxidizing bacteria; EXAFS spectroscopy, extended X-ray absorption fine structure spectroscopy; EPS, exopolysaccharides; SSB, standard-sample bracketing; DS, double spike; PDF, pair distribution function.

* Corresponding author.
E-mail address: elizabeth.swanner@ifg.uni-tuebingen.de (E.D. Swanner).

[1] These authors contributed equally to this work.

http://dx.doi.org/10.1016/j.gca.2015.05.024
0016-7037/

1. INTRODUCTION

Phototrophic Fe(II)-oxidizing bacteria (photoferrotrophs) are able to oxidize Fe(II) in anoxic, sunlit environments. For this reason they are of interest for their potential role in oxidizing Fe(II) in the photic zones of the largely anoxic Archean oceans (e.g., Kappler et al., 2005; Crowe et al., 2008). Iron formations (IF) are Fe-rich chemical sediments that were deposited from Archean seawater and contain mixed-valence Fe minerals. Their overall Fe oxidation state is thought to reflect oxidation and deposition of primary Fe(III) (oxyhydr)oxide phases during deposition (Beukes and Klein, 1992), and subsequent (partial) reduction of these phases during diagenesis by biological or thermogenic Fe(III) reduction with organic carbon (Konhauser et al., 2005; Johnson et al., 2008; Posth et al., 2013a).

While photoferrotrophs might have been involved in Fe(II) oxidation in Archean seawater, there are other possibilities for how Fe(II) might have been oxidized, including photochemical oxidation with UV light, oxidation by microaerophilic Fe(II)-oxidizing bacteria (mFeOB), or direct oxidation by oxygen produced by cyanobacteria (for a recent review see Posth et al., 2013b). However, because abiotic photochemical oxidation is thought to be a very minor Fe(II) oxidation pathway in Si-rich Archean oceans (Konhauser et al., 2007a), much emphasis has been placed on the above-mentioned biological pathways. Of the three types of organisms implicated, only microaerophilic Fe(II)-oxidizing bacteria leave distinct morphological indicators ("biosignatures") of their presence and activity in ancient settings: organic stalks, often twisted, that are coated with Fe(III) minerals (Chan et al., 2011; Krepski et al., 2013). Yet these biosignatures do not appear in the IF record until the late Paleoproterozoic (Cloud, 1965; Planavsky et al., 2009; Wilson et al., 2010), suggesting that microaerophilic FeOB were not involved in Archean Fe(II) oxidation.

As photoferrotrophs do not generate distinctive morphological biosignatures, other traces of their activity should hold more promise for distinguishing their presence and activity in forming IF. Remnants of biological organic molecules ("biomarkers") from these organisms are distinct, and may even be used to distinguish whether photoferrotrophs grew using Fe(II) as an electron donor vs. other reduced compounds (H_2, organics) that are also capable of supporting their growth (Eickhoff et al., 2013). Yet, to date, organic biomarkers have not been successfully isolated out of Fe-rich rocks such as IF. Therefore, other indicators of their activity are needed to distinguish their potential contribution to Archean Fe(II) oxidation and IF deposition.

Fe(II) oxidation and Fe(III) precipitation both cause distinct Fe isotopic fractionations, such that the residual Fe(II) in the aqueous phase ($Fe(II)_{aq}$) has a different isotopic composition from the oxidized, aqueous Fe(III) ($Fe(III)_{aq}$), as well as the Fe(III) (oxyhyr)oxide minerals that rapidly precipitate from $Fe(III)_{aq}$ at circumneutral pH ($Fe(III)_{ppt}$). This difference between the $^{56}Fe/^{54}Fe$ ratios of $Fe(III)_{aq}$ to $Fe(II)_{aq}$ ($\alpha_{Fe(III)_{aq}-Fe(II)_{aq}}$) describes the isotope fractionation of the Fe(II) oxidation process.[2] Because biological enzymes are known to prefer lighter isotopes as substrates, it was initially anticipated that direct, biologically-catalyzed Fe-redox reactions may impart a fractionation between the substrate and product (Beard et al., 1999). In experiments and natural samples of abiotic and biological Fe(II) oxidation at neutral pH, $Fe(III)_{ppt}$, i.e., the product of Fe(II) oxidation, is actually isotopically heavier than $Fe(II)_{aq}$ by about 1–3‰ (Bullen et al., 2001; Balci et al., 2006; Croal et al., 2009; Kappler et al., 2010), due to kinetic effects during rapid precipitation and the formation of stronger bonds in precipitates relative to aqueous phases. If precipitation is slow, equilibrium isotope exchange between $Fe(II)_{aq}$ and $Fe(III)_{aq}$ may be attained, increasing the magnitude of fractionations between $Fe(II)_{aq}$ and $Fe(III)_{ppt}$ (Johnson et al., 2002; Anbar et al., 2005; Balci et al., 2006), but this is not likely significant during rapid precipitation at circumneutral pH. These results imply that Fe isotope composition of minerals precipitated from biological Fe(II) oxidation at circumneutral pH may not be distinguishable from those precipitated abiotically (Balci et al., 2006). A further consideration is that under conditions relevant for ancient oceans, i.e., enhanced Si concentrations, there is isotope exchange between $Fe(II)_{aq}$ and $Fe(III)_{ppt}$ that may overprint the isotopic fractionation associated with Fe(II) oxidation and Fe(III) precipitation (Wu et al., 2012).

Previous work has addressed the role of inorganic ligands (Cl^-, SO_4^{2-}, CO_3^{2-}) in determining the reactivity of different $Fe(II)_{aq}$ species during Fe(II) oxidation (Bullen et al., 2001; Welch et al., 2003; Balci et al., 2006). Equilibrium isotopic exchange between different $Fe(II)_{aq}$ and $Fe(III)_{aq}$ species generally imparts a heavier Fe isotopic composition to the $Fe(III)_{aq}$ phase, but can be influenced by the nature of the dominant ligand (Bullen et al., 2001; Johnson et al., 2002; Balci et al., 2006). The only study to investigate Fe isotopic fractionation by a photoferrotroph utilized a freshwater strain (Croal et al., 2004), yet inorganic ligands such as Cl^-, SO_4^{2-}, SiO_4^{4-}, and PO_4^{3-} are present in both modern and ancient seawater, albeit in variable amounts (Kempe and Degens, 1985; Konhauser et al., 2007b; Canfield and Farquhar, 2009), and should be considered when addressing the role biological Fe(II) oxidation to the isotopic composition of IF.

Furthermore, the role of organic Fe-ligands has only been mentioned in passing in literature that has specifically addressed biological Fe(II) oxidation (Croal et al., 2004; Balci et al., 2006). Yet organics play a critical role in mediating the precipitation of poorly soluble Fe(III) away from the cell surfaces in organisms that oxidize Fe(II) at circumneutral pH (Chan et al., 2004, 2009; Schaedler et al., 2009), and potentially control the isotopic fractionation between pools of $Fe(II)_{aq}$ and particulate Fe(III) phases in marine environments (John et al., 2012; Staubwasser et al., 2013). Spatial separation between the site of oxidation near the cell surface (or within the periplasm) and the site of

[2] The $\alpha_{Fe(III)_{aq}-Fe(II)_{aq}}$ can be converted to an ε value, in per mille (‰), using the equation $\varepsilon_{Fe(III)_{aq}-Fe(II)_{aq}} = (\alpha_{Fe(III)_{aq}-Fe(II)_{aq}} - 1) \times 1000$.

Fe(III) mineral precipitation is critical, because cells that are coated in Fe(III) minerals are not viable if nutrients can no longer diffuse to and from the cell surface (Schmid et al., 2014). While knowledge of the way that microaerophilic FeOB template Fe(III) mineral precipitation along their organic stalks has been unfolding for the last decade (Chan et al., 2004, 2009; Saini and Chan, 2012), it is not entirely clear how phototrophic FeOB prevent encrustation (Schaedler et al., 2009). Previous authors have invoked the presence of a low-pH gradient around the cell that allows $Fe(III)_{aq}$ to diffuse away before precipitating as the pH rises (Hegler et al., 2010). Templating Fe(III) mineral precipitation to extracellular fibers composed of lipopolysaccharides was also suggested as a strategy (Miot et al., 2009), as well as the production of Fe(III)-complexing organic ligands (Kappler and Newman, 2004). Recently, the association of a ligand-bound phase of Fe(III) with excreted exopolymeric substances (EPS) was documented at the site of extracellular mineral formation in laboratory cultures of the marine photoferrotroph *Rhodovulum iodosum* (Wu et al., 2014). It was suggested that excretion of EPS that bind Fe(III) may be a mechanism to move the site of Fe(III) precipitation away from the cell, but the presence of such an intermediate phase may also have implications for the formation of isotopically distinct pools of Fe during microbial Fe(II) oxidation.

Our goal was therefore to discern the role of organic-bound or colloidal Fe phases in the fractionation of Fe isotopes during phototrophic Fe(II) oxidation under marine conditions. To this end we tracked the isotopic composition of Fe in the Fe_{aq} and the Fe_{ppt} phases during batch growth experiments with the marine photoferrotroph *R. iodosum*. To determine the role of a previously inferred Fe(III)-organic phase in Fe isotope fractionation, we conducted extensive characterization of the solid Fe phases that formed during Fe(II) oxidation using Mössbauer spectroscopy, synchrotron-based extended X-ray absorption fine structure (EXAFS) spectroscopy, and X-ray total scattering. Our interpretations on the nature of the soluble, mineral, and intermediate phases present in the system, and their control over the distinct Fe isotopic pools present, were supplemented with particle size and surface area analyses.

2. MATERIALS, METHODS AND MEASUREMENTS

2.1. Bacterial strain and medium

The marine photoferrotroph *R. iodosum* was obtained from Deutsche Sammlung von Mikroorganismen und Zellkulturen (DSMZ), Germany (DSM 12328T). It was isolated from a mud flat of the Jadebusen (North Sea) (Straub et al., 1999). Detailed physiological investigations of this strain have been previously published (Straub et al., 1999; Wu et al., 2014). Marine phototroph (MP) medium was used for cultivation of *R. iodosum*, and Fe(II) was added as previously described (Wu et al., 2014). Here, the medium was filtered anoxically a second time after incubating at 4 °C to ensure all Fe(II) carbonate and phosphate precipitates were removed, as abiotic precipitation of and sorption to Fe(II) in these phases could result in Fe isotope fractionation, and overprint the fractionation of Fe(II) oxidation.

In a glovebox, 80 mL of the Fe(II)-containing MP medium was dispensed into 200 mL capacity serum bottles, and the headspace was flushed with N_2/CO_2 (v/v, 90/10) for 3 min before inoculation. The Fe(II)-containing medium was inoculated from the final incubation of a set of cultures grown first with H_2 as an electron donor, then Fe(II), then H_2. This strategy ensured that the inoculum was adapted to autotrophic growth with Fe(II) as the electron donor, but avoided the introduction of Fe(II)/Fe(III) minerals to the experiments that could contaminate the isotopic measurements. One percent of the culture was inoculated into each experiment, to a final concentration of about 1.5×10^7 cells ml^{-1} (Wu et al., 2014). In each experiment, three parallel bottles (biological replicates) were used for Fe(II) oxidation and isotope fractionation examination, and each had an initial Fe(II) concentration of ca. 4 mM. One abiotic control per experiment was prepared the same but without inoculation. The bottles were incubated at 26 °C and 600 lux (12 μmol quanta m^{-2} s^{-1}) under a 40-W tungsten incandescent light. The light intensity was determined by a Digital Lux Meter (Roline RO1332). The bottles were shaken once by hand every 12 h to avoid attachment of precipitates to the bottle walls.

2.2. Fe species separation, Fe(II) and total Fe concentration determination

During Fe(II) oxidation by *R. iodosum*, Fe was present as several different aqueous or solid species: aqueous Fe(II) or Fe(III) ($Fe(II)_{aq}$ or $Fe(III)_{aq}$), precipitated Fe(II) or Fe(III) minerals ($Fe(II)_{ppt}$ or $Fe(III)_{ppt}$), or as Fe(II) or Fe(III) adsorbed to the minerals, associated with other solid or organic phases (e.g., cell surfaces), or in colloidal forms in the experiment (collectively $Fe(II/III)_{interm}$). To determine the Fe isotope fractionation between these phases during Fe(II) oxidation vs. precipitation or sorption, we analyzed the Fe isotopic composition of total aqueous phase (Fe_{aq}: $Fe(II)_{aq} + Fe(III)_{aq}$), and the total precipitate phase (Fe_{ppt}: $Fe(II)_{ppt} + Fe(III)_{ppt}$ including cells) at approximately 0%, 20%, 40%, 60%, 80% and 100% Fe(II) oxidized from several different experiments with three biological replicates each. During each experiment, samples were removed with a 2 mL syringe inside of an anoxic glovebox (100% N_2). One mL of this anoxically sampled culture was immediately centrifuged inside the glovebox (16,000*g*, 10 min), and the supernatant, containing $Fe(II)_{aq}$ and $Fe(III)_{aq}$, was filtered through a 0.22 μm nylon centrifuge tube filter (Cosar spin-X, Corning, International) and acidified with anoxic 1 M HCl (Fig. 1). The pellet was then washed with anoxic MilliQ water, centrifuged as above, and re-suspended in anoxic 0.5 M sodium acetate (NaAc; pH adjusted to 4.85 with acetic acid), followed by a 24 h incubation in the glove box and centrifugation to separate $Fe(II)_{interm}$ and $Fe(III)_{interm}$, now in the aqueous phase, from the $Fe(II)_{ppt}$ or $Fe(III)_{ppt}$, which remained in the pellet. The Fe concentration and speciation was then measured in these extracted fractions (see below). Finally, the pellet was dissolved in anoxic 6 M HCl to avoid

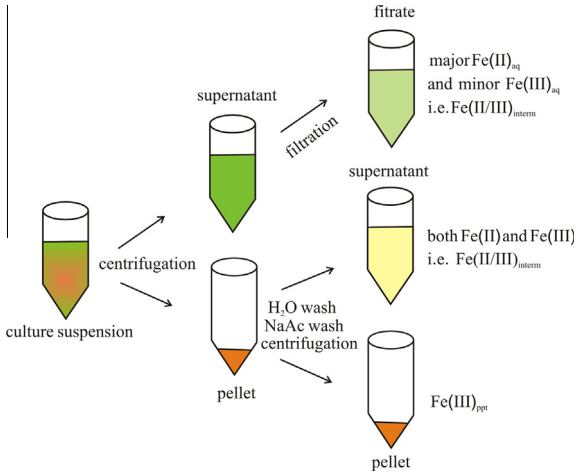

Fig. 1. Schematic detailing the separation procedure for samples taken during oxidation of Fe(II) by *R. iodosum*. The resulting fractions were used for Fe(II) and total Fe determination by Ferrozine, and the Fe isotope composition was determined on the total Fe_{aq} ($Fe(II)_{aq} + Fe(III)_{aq}$) and the total Fe_{ppt} ($Fe(II)_{ppt} + Fe(III)_{ppt}$).

Fe(II) oxidation by O_2 at high Cl^- concentrations under oxic conditions (Porsch and Kappler, 2011). The MilliQ water and NaAc washes were acidified with anoxic 1 M HCl.

We conducted three separate experiments, each with three biological replicates (Table 2). In the first two experiments, *Ri*-1 and *Ri*-2, indicating *R. iodosum* experiment 1 or 2, the aqueous fraction was not separated from the precipitate by filtration, but rather separated simply with centrifugation (16,000*g*, 10 min) (Table 1). Additionally, we did not wash the pellet of samples from *Ri*-1 with NaAc, but did so with all subsequent experiments. The final experiment, *Ri*-3 was filtered and the pellet washed with H_2O and NaAc, and so these results are discussed in the most detail. Clear differences were observed in the Fe isotope composition of the aqueous and precipitate phases in each of the experiments that resulted from the separation protocol, and therefore, we present the results of all experiments to augment the discussion of the role of different Fe phases on the Fe isotope fractionation patterns observed.

The concentration of Fe(II) for all fractions was determined using the Ferrozine assay directly on aqueous or dissolved samples (Stookey, 1970). Total Fe was measured on samples using Ferrozine following treatment with the reducing reagent hydroxylamine hydrochloride (10% wt/v, prepared in 1 M HCl). The Fe(III) concentration was calculated as the difference between the Fe(II) and total Fe of each fraction. Absorption measurements were made using a microtiterplate reader (Analytik Jena Flash Scan 550) at 562 nm. The method has a detection limit of ca. 5–10 μM (0.28–0.56 mg L^{-1}).

2.3. Fe isotope analysis

Iron isotope measurements were made on the Fe_{aq} and Fe_{ppt} fractions (Fig. 1). The concentrations of Fe in the water and NaAc washes were generally very low (<2 μg). Due to limitations in the number of samples that could be processed, the $\delta^{56}Fe$ of the $Fe(II/III)_{interm}$ phases were not measured.

Fe purification work was performed in positively pressured isotope geochemistry clean laboratories at the University of Tuebingen, with class 10,000 HEPA filtered ambient air and class 100 HEPA filtered fume hoods. HNO_3 and HCl used during the digestion of the samples, purification of Fe, or serving as solution matrix for ICP-MS measurements were distilled from p.a. grade acids using individual Savillex© DST 1000 stills. Acid blank levels are constantly checked on each batch of distilled acid before concentration titration and release to laboratory use. All Teflon laboratory ware was carefully cleaned before use by scrubbing with soft sponges and clean laboratory detergent and sequential leaching in hot 3 mol L^{-1} HCl, 5 mol L^{-1} HNO_3, and 18.2 MΩ cm water for 3 days, respectively. Procedural blank levels during sample preparation and chemical purification of Fe were constantly determined together with processed samples. For Fe purification, sample aliquots containing 5 μg of Fe were transferred to PFA Teflon beakers with 1 drop of concentrated HNO_3 to oxidize Fe(II), then dried overnight at 95 °C. The residues were dissolved in 1 mL of 6 mol L^{-1} HCl to ensure conversion of the samples into Fe–Cl complexes and oxidation of all Fe(II) to Fe(III). The samples were purified in Spectrum® 104704 polypropylene columns filled with 1 mL Dowex AG-1x8 100–200 mesh resin. Fe purification followed the anion exchange separation protocol given in Schoenberg and von Blanckenburg (2005). After purification, the samples from *Ri*-2 and *Ri*-3 were dried at 100 °C and repeatedly treated with 100 μL hydrogen peroxide (>30% H_2O_2) to remove residual organics from the resin or the samples themselves (Table 1). The residues were then taken up in 500 μL of 14.5 mol L^{-1} HNO_3 and dried down again to ensure conversion to nitrate form. The samples were finally taken up in 2.5 mL of 0.3 mol L^{-1} HNO_3 and ready for Fe isotope analysis.

Fe isotope analyses were performed in the isotope geochemistry facilities at the University of Tuebingen using a ThermoFisher Scientific NeptunePlus Multi-collector inductively coupled plasma mass spectrometer (MC-ICP-MS). Polyatomic interferences, such as $^{40}Ar^{14}N^+$ on $^{54}Fe^+$ or

Table 1
Fe separation and isotope measurement protocol for the three experiments.

Experiment	Date	Supernatant centrifuged or filtered	H_2O wash	NaAc wash	H_2O_2 treatment	SSB or double spike
Ri-1	December 2012	Centrifuged	Yes	No	No	SSB
Ri-2	February 2013	Centrifuged	Yes	Yes	Yes	SSB
Ri-3	July 2013	Filtered	Yes	Yes	Yes	Both

Table 2
Iron isotope data from experiments with *R. iodosum*. Each sample was measured twice. Parameters for the Rayleigh fit of $\delta^{56}Fe_{aq}$ or $\delta^{56}Fe_{ppt}$ from each replicate are reported, as well as the equilibrium fit for all replicates from each experiment. Samples from *Ri*-3 were measured twice, once with standard-sample bracketing (SSB) and once with a double spike (DS).

Experiment	Replicate	Day	Fraction of Fe(II) oxidized	$\delta^{56}Fe_{aq}$ (‰)	2SD	$\delta^{56}Fe_{ppt}$ (‰)	2SD
Ri-1 (SSB)	1	0	0.00	−0.056	0.200	NM	NM
	1	8	0.18	0.035	0.050	NM	NM
	1	12	0.22	0.014	0.069	0.644	0.050
	1	17	0.33	NM	NM	0.950	0.098
	1	22	0.41	−0.252	0.050	1.679	0.051
	1	25	0.86	−1.490	0.050	0.364	0.083
$\varepsilon_{Fe(II/III)interm-Fe(II)aq} = 0.682‰$, $\sum chi^2 = 0.129$; $\varepsilon_{Fe(III)ppt-Fe(III)aq} = 1.344‰$, $\sum chi^2 = 0.758$							
Ri-1 (SSB)	2	0	0.00	−0.074	0.050	NM	NM
	2	8	0.17	0.048	0.050	NM	NM
	2	12	0.21	0.046	0.050	0.630	0.050
	2	17	0.31	−0.035	0.069	1.323	0.050
	2	22	0.83	−1.093	0.050	0.414	0.050
	2	25	1.00	NM	NM	0.000	0.050
$\varepsilon_{Fe(II/III)interm-Fe(II)aq} = 0.550‰$, $\sum chi^2 = 0.136$; $\varepsilon_{Fe(III)ppt-Fe(III)aq} = 1.177‰$, $\sum chi^2 = 0.292$							
Ri-1 (SSB)	3	0	0.00	0.007	0.053	NM	NM
	3	12	0.12	0.028	0.075	NM	NM
	3	17	0.41	−0.458	0.063	NM	NM
	3	25	1.00	NM	NM	−0.002	0.127
$\varepsilon_{Fe(II/III)interm-Fe(II)aq} = ND$; $\varepsilon_{Fe(III)ppt-Fe(III)aq} = ND$							
Equilibrium Fits *Ri*-1 (SSB): $\delta^{56}Fe_{aq} = -1.14X - 0.04$, $\sum chi^2 = 0.911$; $\delta^{56}Fe_{ppt} = -1.49X + 1.44$, $\sum chi^2 = 1.574$							
Ri-2 (SSB)	1	0	0.00	−0.025	0.056	NM	NM
	1	10	0.10	−0.074	0.059	NM	NM
	1	12	0.28	−0.304	0.056	2.053	0.061
	1	13	0.44	−0.945	0.053	1.325	0.071
	1	17	0.97	NM	0.079	0.007	0.064
$\varepsilon_{Fe(II/III)interm-Fe(II)aq} = 0.682‰$, $\sum chi^2 = 0.129$; $\varepsilon_{Fe(III)ppt-Fe(III)aq} = 1.344‰$, $\sum chi^2 = 0.758$							
Ri-2 (SSB)	2	0	0	−0.001	0.064	NM	NM
	2	5	0.04	−0.018	0.062	NM	NM
	2	10	0.35	−0.657	0.066	1.563	0.057
	2	12	0.96	−2.547	0.071	0.125	0.068
	2	17	0.96	NM	NM	−0.042	0.071
$\varepsilon_{Fe(II/III)interm-Fe(II)aq} = 1.493‰$, $\sum chi^2 = 12.597$; $\varepsilon_{Fe(III)ppt-Fe(III)aq} = 1.878‰$, $\sum chi^2 = 0.097$							
Ri-2 (SSB)	3	0	0.00	0.017	0.063	NM	NM
	3	5	0.07	−0.007	0.058	NM	NM
	3	10	0.22	−0.116	0.058	1.786	0.054
	3	12	0.59	−1.054	0.062	1.045	0.059
	3	17	0.95	NM	NM	−0.023	0.053
$\varepsilon_{Fe(II/III)interm-Fe(II)aq} = 0.400‰$, $\sum chi^2 = 4.221$; $\varepsilon_{Fe(III)ppt-Fe(III)aq} = 1.872‰$, $\sum chi^2 = 0.133$							
Equilibrium Fits *Ri*-2 (SSB): $\delta^{56}Fe_{aq} = -2.21X - 0.003$, $\sum chi^2 = 0.733$; $\delta^{56}Fe_{ppt} = -2.49X + 2.49$, $\sum chi^2 = 0.388$							
Ri-3 (SSB)	1	0	0.00	0.064	0.050	NM	NM
	1	3	0.14	0.184	0.050	NM	NM
	1	7	0.19	0.147	0.050	NM	NM
	1	9	0.22	−0.046	0.050	2.142	0.050
	1	10	0.34	−0.165	0.050	NM	NM
	1	11	0.44	−0.580	0.050	1.323	0.050
	1	13	1.00	NM	NM	0.120	0.050
$\varepsilon_{Fe(II/III)interm-Fe(II)aq} = 0.459‰$, $\sum chi^2 = 0.216$; $\varepsilon_{Fe(III)ppt-Fe(III)aq} = 2.218‰$, $\sum chi^2 = 0.165$							
Ri-3 (SSB)	2	12	0.58	−0.997	0.034	1.051	0.037
$\varepsilon_{Fe(II/III)interm-Fe(II)aq} = ND$; $\varepsilon_{Fe(III)ppt-Fe(III)aq} = ND$							
Ri-3 (SSB)	3	3	0.11	0.173	0.050	NM	NM
	3	9	0.18	NM	NM	1.983	0.050
	3	10	0.30	−0.203	0.050	1.910	0.050
	3	11	0.45	NM	NM	1.328	0.050
	3	12	0.82	−2.063	0.050	0.581	0.050

(*continued on next page*)

Table 2 (*continued*)

Experiment	Replicate	Day	Fraction of Fe(II) oxidized	$\delta^{56}Fe_{aq}$ (‰)	2SD	$\delta^{56}Fe_{ppt}$ (‰)	2SD
$\varepsilon_{Fe(II/III)interm-Fe(II)aq} = 1.219‰$, $\sum chi^2 = 0.095$; $\varepsilon_{Fe(III)ppt-Fe(III)aq} = 2.012‰$, $\sum chi^2 = 0.141$							
Equilibrium Fits *Ri*-3 (SSB): $\delta^{56}Fe_{aq} = -2.21X + 0.06$, $\sum chi^2 = 1.174$; $\delta^{56}Fe_{ppt} = -2.47X + 2.53$, $\sum chi^2 = 0.290$							
Ri-3 (DS)	1	0	0.00	0.061	0.030	NM	NM
	1	3	0.14	0.103	0.030	NM	NM
	1	7	0.19	0.079	0.030	NM	NM
	1	9	0.22	−0.058	0.030	1.991	0.030
	1	10	0.34	−0.284	0.030	1.749	0.030
	1	11	0.44	−0.669	0.030	1.206	0.030
	1	12	0.91	−2.242	0.030	0.494	0.030
$\varepsilon_{Fe(II/III)interm-Fe(II)aq} = 0.956‰$, $\sum chi^2 = 0.134$; $\varepsilon_{Fe(III)ppt-Fe(III)aq} = 1.975‰$, $\sum chi^2 = 0.151$							
Ri-3 (DS)	2	10	0.24	NM	NM	1.982	0.030
	2	12	0.58	−0.977	0.030	1.017	0.030
	2	13	0.96	−3.494	0.030	NM	NM
$\varepsilon_{Fe(II/III)interm-Fe(II)aq}$ = ND; $\varepsilon_{Fe(III)ppt-Fe(III)aq}$ = ND							
Ri-3 (DS)	3	3	0.11	0.105	0.030	NM	NM
	3	9	0.18	NM	NM	1.988	0.030
	3	10	0.30	−0.243	0.030	1.797	0.030
	3	11	0.45	NM	NM	1.314	0.030
	3	12	0.82	−1.985	0.030	0.541	0.030
$\varepsilon_{Fe(II/III)interm-Fe(II)aq} = 1.180‰$, $\sum chi^2 = 0.049$; $\varepsilon_{Fe(III)ppt-Fe(III)aq} = 1.962‰$, $\sum chi^2 = 0.135$							
Equilibrium Fits *Ri*-3 (DS): $\delta^{56}Fe_{aq} = -2.55X + 0.06$, $\sum chi^2 = 1.668$; $\delta^{56}Fe_{ppt} = -2.42X + 2.48$, $\sum chi^2 = 0.365$							

NM = sample not measured. ND = not determined because there were too few data points for fitting.

$^{40}Ar^{16}O^{+}$ on $^{56}Fe^{+}$ were resolved using the high mass-resolution mode of the mass spectrometer and instrumental mass bias was accounted for by using the standard-sample-bracketing (SSB) method. Run conditions during SSB measurements followed the protocol given in Schoenberg and von Blanckenburg (2005). To verify the lack of any effects on the sample's true Fe isotopic compositions during chemical purification and mass spectrometric analyses, one experiment (*Ri*-3) was additionally measured with a double spike (DS) method. For this, an adequate amount of an isotopically enriched tracer solution (i.e., an ^{57}Fe–^{58}Fe double spike) was homogenized with all samples and standards prior to chemical Fe purification via anion exchange chromatography. The Fe double spike allows correction of any mass-dependent isotopic fractionation during Fe purification, as may be induced by the organic sample matrices affecting the purification yield, but it also accounts for the instrumental mass bias or any mass-dependent effects on it by residual organic compounds in the Fe analyte (Schoenberg and Von Blanckenburg, 2005). Both these effects by organic compounds would remain undetected by the SSB measuring method, potentially compromising the results. As for SSB measurements, all four Fe isotope beams were detected simultaneously during DS runs, which consisted of 90 integration cycles at 8 s. Background corrections for sample signals were based on on-peak-zero measurements on the pure analyte solution prior to each sample analysis. Data are reported in the δ-notation with units of per mille (‰) relative to the isotopically certified international reference material IRMM-014 (Institute for Reference Materials and Measurements in Gent, Belgium):

$$\delta^{56}Fe = \left(^{56}Fe/^{54}Fe_{sample}/^{56}Fe/^{54}Fe_{IRMM\text{-}014} - 1\right) \times 1000$$

The reproducibility of HanFe standard measurements that were run with the SSB method during the course of this study was 0.296 ± 0.039‰ (2SD; $n = 13$), which compares well to the long-term reproducibility of 0.287 ± 0.055‰ (2SD; $n = 145$) for this standard. The reproducibility of the IRMM-014 and HanFe standard measurements that were run with the double-spike method during the course of this study were −0.007 ± 0.018‰ (2SD; $n = 8$) and 0.279 ± 0.030‰ (2SD; $n = 5$), respectively.

The $\delta^{56}Fe$ values of Fe_{aq} and Fe_{ppt} at different fractions (f) of Fe(II) remaining from individual biological replicates were fit with a Rayleigh equation:

$$\delta^{56}Fe_{aq} = \left(\delta^{56}Fe_{aq\text{-}0} + 100\right) \times f^{\alpha-1} - 1000 \quad (1)$$

$$\delta^{56}Fe_{ppt} = \left(\delta^{56}Fe_{aq\text{-}0} + 1000\right) \times [(1 - f^{\alpha})/(1 - f)] - 1000 \quad (2)$$

The α values were determined by minimizing the sum of chi^2 values using the Solver tool in Microsoft Excel, where the sum of chi^2 values was determined by comparing the fit to either the $\delta^{56}Fe_{aq}$ or the $\delta^{56}Fe_{ppt}$ dataset. The α values were converted to per mille units via the following equation:

$$\varepsilon = (\alpha - 1) \times 1000 \quad (3)$$

Data from all three replicates of each experiment were fit with a linear equation optimized in Solver by minimizing the sum of chi^2 values to determine the equilibrium equation. The intercept of the $\delta^{56}Fe_{aq}$ linear fit was fixed as the initial measured $\delta^{56}Fe_{aq}$, and the $\delta^{56}Fe_{ppt}$ fit had to reach the initial $\delta^{56}Fe_{aq}$ when all Fe had been oxidized.

Because the Fe isotopic composition of intermediate Fe phases ($Fe(II/III)_{interm}$), present in the water and NaAc washes was not measured, we used a mass balance approach to calculate it:

$$f_{interm} * \delta^{56}Fe(II/III)_{interm}(t) = 1 * \delta^{56}Fe_{aq}(initial) - f_{aq} * \delta^{56}Fe_{aq}(t) - f_{ppt} * \delta^{56}Fe_{ppt}(t) \quad (4)$$

In the above expressions, f represents the fraction of total Fe in the experiment that is in each phase, designated by the subscript. The initial $\delta^{56}Fe_{aq}$ was determined from the first sample, taken at the beginning of each experiment. At each time point where both data $\delta^{56}Fe_{aq}$ and $\delta^{56}Fe_{ppt}$ were measured from the first replicate of the *Ri*-3 DS dataset (Fig. 1, Table 2), this equation was used to solve for $\delta^{56}Fe(II/III)_{interm}$.

2.4. Mineralogy

2.4.1. Mössbauer spectroscopy

Solids produced when about 40% of Fe(II) had been oxidized by *R. iodosum* were collected, washed with anoxic MilliQ water and air-dried in an anoxic glovebox (100% N_2). Samples were prepared by loading dry powders into Plexiglas® holders (area 1 cm^2). The mass of each sample (approximately 10 mg) was mixed with 80 mg glucose monohydrate (Roth, Germany) to ensure a homogenous sample with ideal thickness. The samples were inserted into a close-cycle exchange gas cryostat (Janis cryogenics). Spectra were collected at 295, 77 and 5 K using a constant acceleration drive system (WissEL) in transmission mode with a ^{57}Co/Rh source and calibrated against a 7 μm thick α-^{57}Fe foil measured at room temperature. Spectra were analyzed using Recoil (University of Ottawa) with a Voigt based fitting (VBF) routine (Rancourt and Ping, 1991).

2.4.2. Synchrotron-based X-ray absorption spectroscopy (XAS)

The solid product of Fe(II) oxidation by *R. iodosum* following complete Fe(II) oxidation was collected in a glovebox and washed with marine phototroph medium that contained no nutrients (no phosphate, nitrate, vitamins, trace elements or bicarbonate). The sample was transported wet and without exposure to oxygen to the synchrotron beamline, then loaded into a Teflon sample holder inside a glovebox, sealed with Kapton tape, and frozen. This sample was then loaded into a liquid N_2-cooled cryostat to maintain original oxidation state during analysis.

Bulk mineralogy was investigated with Fe K-edge Extended X-ray Absorption Fine Structure (EXAFS) spectroscopy on Beamline 4-1 at the Stanford Synchrotron Radiation Lightsource (SSRL) using a 13-element germanium detector in fluorescence mode. The spectrum was calibrated by adjusting the E_0 of an Fe foil placed in line with the sample to 7112 eV. The spectrum was deadtime corrected, averaged, and fit with reference spectra using modules in the SIXpack software package (Webb, 2005). The spectrum was corrected for self-absorption using structural constraints for ferrihydrite (Michel et al., 2007a). Using the cycle fit function of the least squares fit (LSF) module in SIXpack, the best fitting Fe reference spectra from a dataset of Fe(III) (oxyhydr)oxides and Fe(III)-organic complexes were determined (lowest reduced chi^2). The spectrum was then fit with combinations of these reference spectra that accounted for greater than 5% of the fit, up to a total of 100%. One reference spectra used in the final fit was synthetic 2-line ferrihydrite with a Si:Fe of 3×10^{-4} synthesized according to the method of Schwertmann and Cornell (2000). This synthetic ferrihydrite was analyzed as a powder held in a window of a Teflon holder with Kapton tape in fluorescence and transmission mode on BL4-1 using a Lytle detector. The mineralogy (2-line ferrihydrite) was verified by XRD at the University of Colorado (Swanner et al., 2011).

2.4.3. Synchrotron-based X-ray total scattering

High energy synchrotron X-ray scattering experiments were performed on the solid products of Fe(II) oxidation by *R. iodosum* at the Advanced Photon Source at Argonne National Laboratory, Beamline 11-ID-B. The solids were collected from a culture grown with ca. 4 mM Fe(II), washed five times with Millipore water to remove excess salt, and analyzed in air in a hydrated state while held in a 1.5 mm O.D. Kapton® capillary. The incident X-ray energy was fixed at 58.3 keV ($\lambda = 0.2128$ Å) and the scattered radiation from the sample suspension and water blank was collected in transmission mode using a Perkin Elmer™ amorphous silicon area detector (2048 × 2048 pixels, 200 × 200 μm^2 pixel size). A CeO_2 standard (NIST diffraction standard set 674a) was used to calibrate the sample-to-detector distance and the non-orthogonality of the detector relative to the incident beam path. The raw scattering data was processed into spectra using the Fit 2D software (Hammersley, 1998). A polarization correction was applied during integration of the data. The total structure function ($S(Q)$), reduced structure function ($Q[S(Q) - 1]$), and the reduced atomic pair distribution function (PDF, $G(r)$) were extracted from the experimental data using PDFgetX2 (Qiu et al., 2004).

2.4.4. Particle analysis

Culture suspensions of *R. iodosum* after Fe(II) was fully oxidized were analyzed for particle size with a Mastersizer 2000 (Malvern Instruments GmbH). The surface area of solids was analyzed using a Micromeritics ASAP 2000 BET analyzer. Elemental composition of particles was measured on a Thermo Scientific Element2 ICP-MS at the European Institute for Marine Studies, France. Element concentrations were determined on solids after cultures reached stationary phase.

3. RESULTS

3.1. Fe speciation during Fe(II) oxidation

The amount of Fe(II), total Fe and Fe(III) in each of the separate fractions [aq, interm (H_2O and NaAC), and ppt] are plotted for the second replicate from the experiment *Ri*-3 (SSB/DS) in Fig. 2, the experiment for which Fe

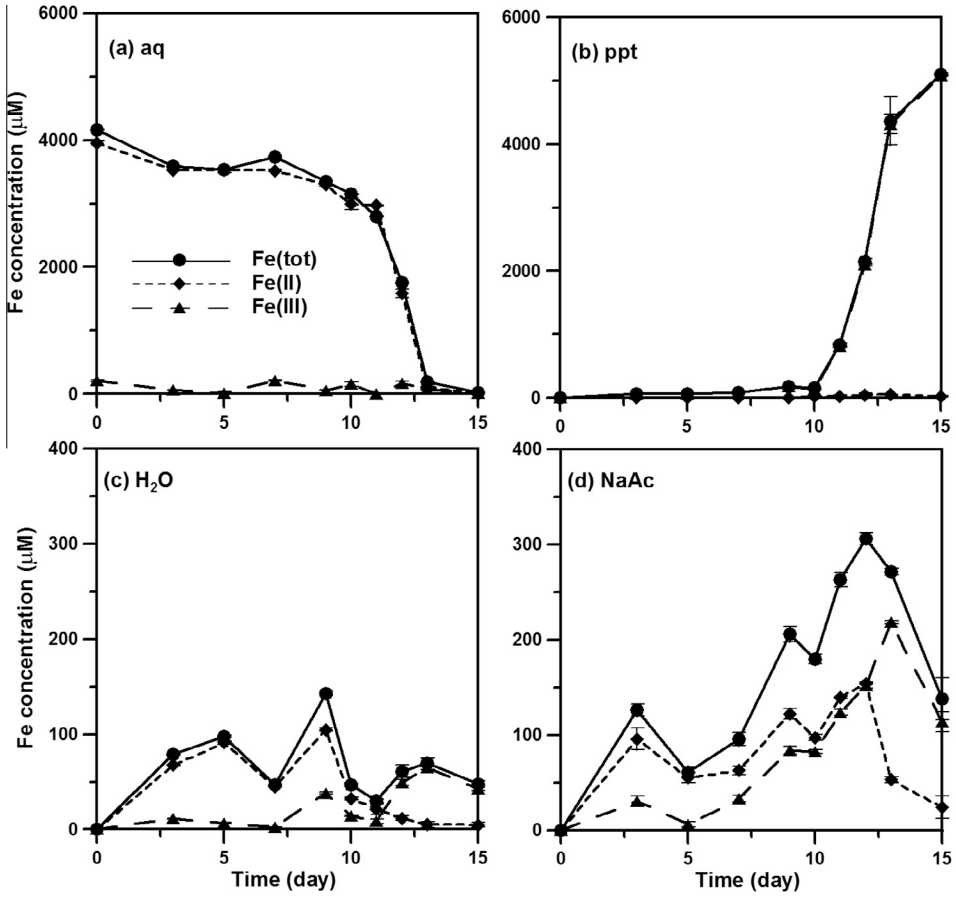

Fig. 2. Fe(II), Fe(III), and total Fe determined for (a) the aqueous Fe fraction (Fe_{aq}), (b) the precipitated fraction (Fe_{ppt}), (c) the H_2O-washed fraction, and (d) the NaAc-washed fraction at different time points during an Fe(II) oxidation experiment with *R. iodosum*. The data shown are from the second biological replicate of experiment *Ri*-3, from which the $\delta^{56}Fe$ of the $Fe(II/III)_{interm}$ phase was calculated using the DS data. Error bars show the standard error of the mean of replicated measurements.

concentrations were determined on samples from the four different phases at all time points (note that Fe isotopes were measured on only a subset of time points and samples; see Table 2). Fe concentration data for all other experiments and replicates is reported in Supplementary Table 1. There was up to a few hundred μM $Fe(III)_{aq}$ in the Fe_{aq} samples (generally less than 10% of the total Fe in the bottle), so we will refer to the total Fe_{aq} phase (Fe(II) + Fe(III)) rather than an $Fe(II)_{aq}$ phase for isotopic measurements. Our measurements indicate that there was no $Fe(II)_{ppt}$ at any point in the experiments. However, a minor amount of $Fe(II)_{interm}$ (5–10% of total Fe in the bottle) was present during the first half of Fe(II) oxidation, while the intermediate fraction was dominated by Fe(III) in the second half of oxidation (Fig. 2; Supplementary Table 1). The average maximum oxidation rates for each biological replicate were calculated from linear regression of three datapoints that define the steepest part of $Fe(II)_{aq}$ vs. time curves, such as that presented in Fig. 2. The rate for *Ri*-1 was 1.26 ± 0.09 mM day^{-1}, 0.89 ± 0.05 mM day^{-1} for *Ri*-2, and 0.61 ± 0.09 mM day^{-1} for *Ri*-3 (error is standard error of the mean, SEM). These results are similar to the previously reported rate for *R. iodosum* (1.27 mM day^{-1} with 4.07 mM initial Fe(II)) (Wu et al., 2014).

3.2. Fe isotope results

The $\delta^{56}Fe$ values for the three separate experiments (*Ri*-1, *Ri*-2, and *Ri*-3) and the three biological replicates of each experiment are presented in Table 2. Samples from experiment *Ri*-3 were measured twice; once with SSB and then again with a DS. The results of the two methods are highly correlated ($R = 0.99882$; Supplementary Fig. 1), indicating that the SSB measurements of our samples were not affected by matrix interferences or instrumental mass bias effects by residual organic compounds in the analyte solutions. Procedural blanks determined during column purification varied between 21 and 42 ng Fe, and are negligible compared to the amount of sample passed through the Fe purification procedure.

The ε determined for the $\delta^{56}Fe_{aq}$ data using a kinetic Rayleigh fractionation model ranged from 0.40‰ (*Ri*-2, 3rd replicate) to 1.49‰ (*Ri*-2, 2nd replicate) for SSB measurements, and 0.96‰ (*Ri*-3, 1st replicate) to 1.18‰ (*Ri*-3, 3rd replicate) for DS measurements (gray areas in Fig. 3). This calculation makes an assumption that all aqueous Fe was present as $Fe(II)_{aq}$, which was not the case in our experiments (Fig. 2; Supplementary Table 1). The $\delta^{56}Fe_{ppt}$ data were also fit using a Rayleigh model, in which Fe_{ppt}

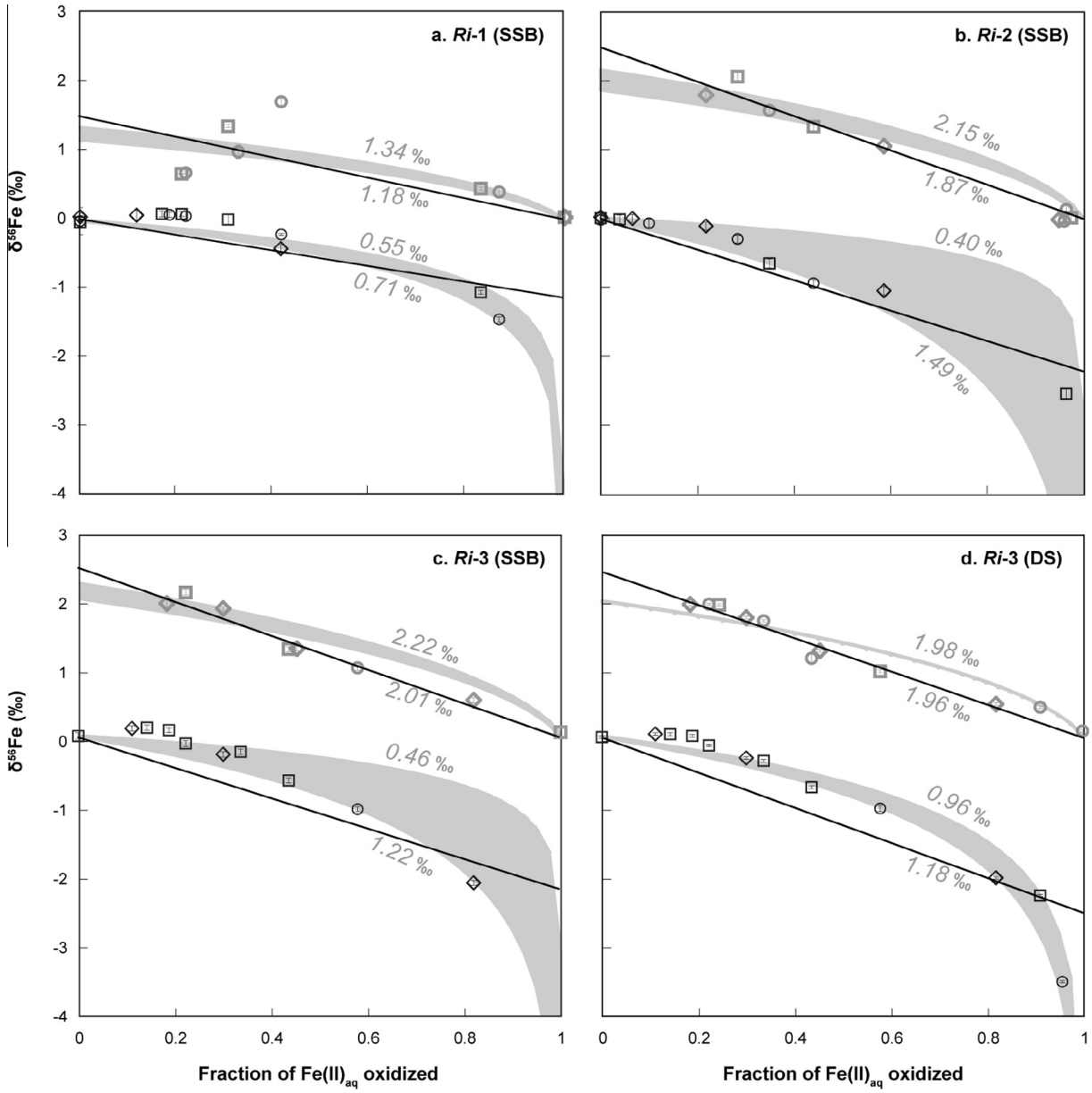

Fig. 3. Evolution of $\delta^{56}Fe_{aq}$ (black symbols) and $\delta^{56}Fe_{ppt}$ (gray symbols) during Fe(II) oxidation by *R. iodosum* from (a) *Ri*-1 (SSB), (b) *Ri*-2 (SSB), (c) *Ri*-3 (SSB), and (d) *Ri*-3 (DS). Different symbol shapes denote the separate biological replicates for each experiment (see Table 2). The gray areas define the range of ε values (labeled) for Rayleigh fits to either $\delta^{56}Fe_{aq}$ or $\delta^{56}Fe_{ppt}$ data points of each of three biological replicate. The black lines are equilibrium fits to either the $\delta^{56}Fe_{aq}$ or $\delta^{56}Fe_{ppt}$ data from each experiment.

forms directly from Fe_{aq}. However, the $\varepsilon_{Feppt-Feaq}$ values derived from fits of these data points were generally larger than those determined from Rayleigh fits of the $\delta^{56}Fe_{aq}$ data, from 1.17‰ (*Ri*-1 2nd replicate) to 2.22‰ (*Ri*-3 1st replicate) for SSB measurements, and 1.96‰ (*Ri*-3 3rd replicate) to 1.98‰ (*Ri*-3 1st replicate) for DS measurements. The ε and sum of chi^2 values for Rayleigh fits for each Fe fraction (Fe_{aq} or Fe_{ppt}) for each replicate of each experiment are listed in Table 2. To evaluate the possibility of equilibrium isotope fractionation, the $\delta^{56}Fe_{aq}$ data from all replicates of each experiment were additionally fit with an equilibrium (linear) model (black lines in Fig. 3). Independent equilibrium fits were made to the $\delta^{56}Fe_{ppt}$ data. The best fit lines and sum of chi^2 values for equilibrium fits are reported in Table 2.

3.3. Fe mineralogy

We used three different methodologies to determine the mineralogy and coordination environment of Fe in the solid Fe samples: ^{57}Fe Mössbauer spectroscopy, EXAFS, and X-ray total scattering/PDF analysis. ^{57}Fe Mössbauer spectra were collected at 295, 77 and 5 K on a washed and anoxically dried sample of the mineral phases after about 40% of

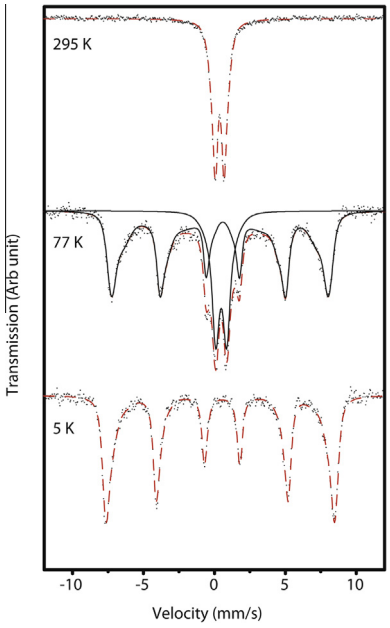

Fig. 4. ^{57}Fe Mössbauer spectra were collected at 295, 77 and 5 K for the anoxically dried solid Fe phase after 40% of Fe(II) oxidation had been oxidized by *R. iodosum*. Data points correspond to the raw data, the dashed lines correspond to the fits of the data, and the lines correspond to the sub-spectra of the fit determined at 77 K.

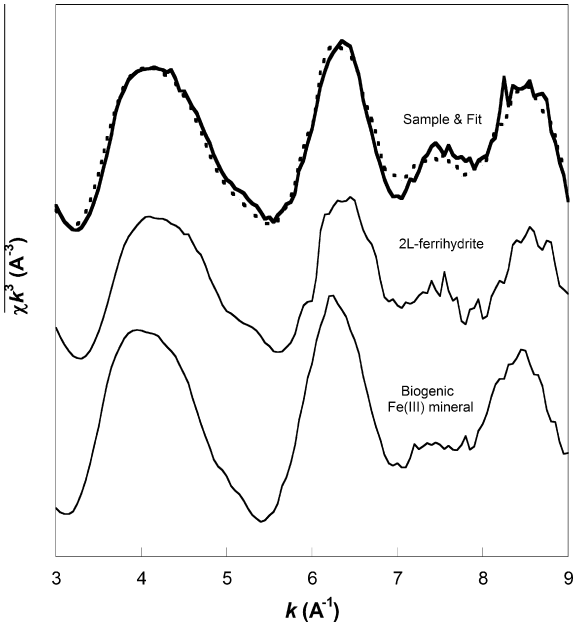

Fig. 5. Fe K-edge EXAFS spectrum of the solid Fe phase formed after complete Fe(II) oxidation by *R. iodosum* (top solid line) and fit (dashed line). The spectrum was best fit with 2-line ferrihydrite synthesized in the presence of Si and a biogenic Fe(III) mineral from an Fe(II)-oxidizing microbial mat from a seafloor hydrothermal vent (Toner et al., 2009b).

the Fe(II) had oxidized (Fig. 4). The room temperature (295 K) spectrum is characterized by the presence of one doublet with a truncated base. The center shift and quadrupole splitting of this doublet are characteristic of a poorly crystalline Fe(III) mineral phase, which likely corresponds to ferrihydrite (Table 3) (Murad, 2010). The doublet showed a broadened linewidth (0.198 mm/s) in comparison to a sample of synthetic ferrihydrite (0.137 mm/s), which was also measured at 295 K. Lower temperature measurements (77 K) indicate the emergence of a sextet, which is indicative of superparamagnetic behavior in the dried solid sample. At 5 K, the sextet is clearly defined and the doublet is no longer visible, indicating the sample is fully magnetically ordered at 5 K.

Two reference spectra were used to fit the Fe EXAFS spectrum of the wet, washed solid Fe phase collected after complete Fe(II) oxidation by *R. iodosum* (Fig. 5). Forty-seven percent of the fit was made up of a spectrum for a biogenic Fe(III) (oxyhydr)oxide mineral collected from an Fe(II)-oxidizing microbial mat at a seafloor hydrothermal vent (Toner et al., 2009b). The remaining 54% of the fit was made from a 2-line ferrihydrite synthesized in the presence of Si. The fit had a reduced chi^2 of 0.15.

High-energy total scattering data were collected at room temperature on the wet, washed solid Fe phase after complete oxidation by *R. iodosum*. The PDF (Fig. 6) obtained from the total scattering data of the sample was compared to the experimental PDFs of pure synthetic 2-line ferrihydrite and a natural, Si-rich biogenic Fe(III) (oxyhydr)oxide mineral. Similarities in the positions of features at $r = \sim 2$ Å and $4 < r < 7$ Å in the sample compared with 2-line ferrihydrite suggest that the sample contains a ferrihydrite-like Fe phase. However, the increased attenuation in the PDF amplitudes with increasing r-values indicates that the

Table 3
^{57}Fe Mössbauer fitting parameters obtained at temperatures 295, 77 and 5 K for solid Fe phases produced by *R. iodosum* after 40% of Fe(II) had been oxidized. CS – Center shift, ΔE_Q – Quadrupole splitting, ϵ – Quadrupole shift, H – magnetic hyperfine field, Pop. – relative population–, χ^2 – error of the fit.

Sample	Temp. (K)		<CS> (mm/s)	<ΔE_Q> (mm/s)	<ϵ> (mm/s)	<H> (T)	Pop. (%)	±	χ^2
Ferrihydrite	295	D	0.35	0.72			100.0		0.94
Sample	295	D	0.38	0.74			100.0		0.70
	77	D	0.48	0.98			27.9	3.0	0.68
		S	0.50		−0.10	40.8	72.1	3.0	
	5	S	0.49		−0.06	48.5	100.0		0.56

sample has a lesser degree of structural order and/or smaller particle size compared with 2-line ferrihydrite. Other differences between the sample and 2-line ferrihydrite are apparent, for example, the positions and amplitudes of the features between 2.5 and 4 Å. Overall, the sample PDF is remarkably similar to the PDF from the Si-rich biogenic Fe(III) (oxyhydr)oxide mineral collected from an Fe(II)-oxidizing microbial mat at a seafloor hydrothermal vent (Toner et al., 2012). The main exception is the peak in the sample PDF at 1.53 Å, which is slightly offset from that at 1.61 Å, the longer distance indicative of an Si–O bond (Toner et al., 2012). The peak at 1.53 Å in the sample PDF is assigned to phosphate based on the average P–O bond distance (Shannon, 1976).

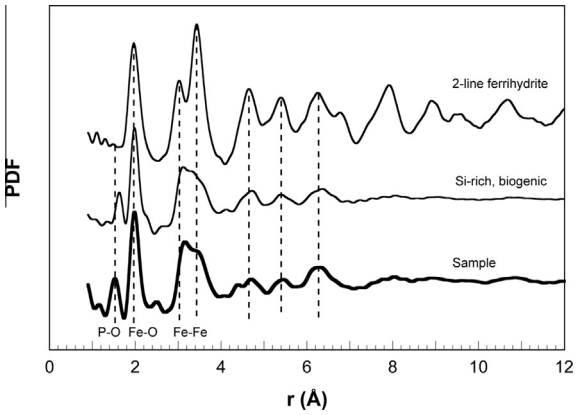

Fig. 6. PDF obtained from the X-ray total scattering data for the Fe solid produced after complete Fe(II) oxidation by *R. iodosum* (thick black spectra). Also shown are PDF from reference phases: 2-line ferrihydrite (Michel et al., 2007b) and a Si-rich biogenic Fe(III) mineral from an Fe(II)-oxidizing microbial mat from a seafloor hydrothermal vent (Toner et al., 2012). Peaks at 1.53 and 1.98 Å in the sample correspond to P–O and Fe–O bonds. Peaks at 3 and 3.45 Å in 2-line ferrihydrite are dominated by Fe–Fe contributions (Michel et al., 2010).

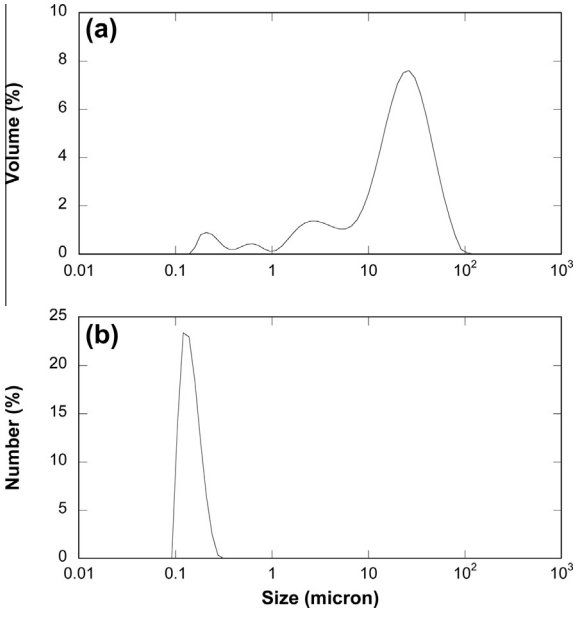

Fig. 7. (a) 94% of the volume of all particles present in the total culture suspension after complete Fe(II) oxidation by *R. iodosum* were distributed between 0.1 and 100 μm in diameter. (b) However, 99.7% of particles in the system were <1 μm in diameter. Note that *R. iodosum* cells are ca. 1 μm long.

The majority of particles present in the entire culture suspension after complete Fe(II) oxidation were between 40 and 300 nm in diameter. Fewer than 1% of particles between 1 and 100 μm in diameter represented 94% of the volume fraction, while more than 99% of the particles were smaller than 1 μm (Fig. 7). The average surface area of the particles (or particle aggregates) was 126.0 ± 0.5 m^2 g^{-1}.

4. DISCUSSION

4.1. Fe isotope fractionation during Fe(II) oxidation by *R. iodosum* – evidence for an isotopically light Fe(II/III)$_{interm}$ phase

The results of our accumulated dataset of $\delta^{56}Fe_{aq}$ and $\delta^{56}Fe_{ppt}$ from biological and analytical replicates measured by SSB and DS methods tell a coherent story: that the pool of Fe_{aq} becomes isotopically lighter as Fe(II) oxidation progresses, consistent with production of an isotopically heavier phase during precipitation of Fe(III) (Fig. 3). Several observations from the variable separation protocols of our experiments (Table 1) suggest a suitable methodology for collecting and purifying samples for Fe isotope analysis from these types of biological samples. The $\delta^{56}Fe_{ppt}$ values in the first half of Fe(II) oxidation in experiment *Ri*-1, the experiment in which Fe_{ppt} was not washed with NaAc, were lighter than in subsequent experiments (Fig. 3a). It is likely that the solid in the beginning of the first experiment included some isotopically lighter phase, possibly adsorbed Fe_{aq} (Fig. 1). After completion of experiment *Ri*-1, we modified our separation protocol to include a NaAc wash of the Fe_{ppt}, resulting in heavier initial Fe_{ppt} values in *Ri*-2 and subsequent experiments as compared to *Ri*-1. The Fe concentration data from the NaAc wash reveals that Fe(II) is the predominant sorbed species initially, suggesting the isotopically light component may be sorbed Fe(II) (Fig. 2 and Supplementary Table 1). Previous workers ruled out isotopic fractionation during extraction with NaAc (Crosby et al., 2007). Similar evidence for the presence of a light Fe component in Fe_{ppt} was observed in the initial Fe(II) oxidation stages of previous biological Fe(II) oxidation experiments that were separated by centrifugation only (their Fig. 4; Kappler et al., 2010), or in experiments where the precipitate was not washed with NaAc (their Fig. 6; Croal et al., 2004). We recommend that future work include both filtration with 0.22 μm filters and washing of the precipitate with NaAc based on collected results from those prior studies. Rayleigh fits of Fe_{aq} in experiments that were filtered (i.e., *Ri*-3) rather than centrifuged (i.e., *Ri*-1 and *Ri*-2) had larger α values derived from fits (Table 2), suggesting that filtration removes isotopically heavier micro-particles from the $Fe(II)_{aq}$ solution, which evade separation from the liquid by centrifugation.

As all Fe separation protocols were carried out on samples from *Ri*-3 (Table 1), and these samples also had the best Fe recovery of all experiments (Supplementary Table 1), we focus on this dataset for evaluating fits of the Rayleigh (kinetic) vs. equilibrium models. We observed a clear distinction between the range of ε values calculated by the Rayleigh model for biological replicates from the $\delta^{56}Fe_{aq}$ data (0.96–1.18‰ for DS measurements) vs. from the $\delta^{56}Fe_{ppt}$ data (1.96–1.98‰ for DS measurements), indicating that Fe(II) oxidation and Fe(III) precipitation in our experiments cannot be described by a single kinetic fractionation process. However, the Rayleigh equation for $\delta^{56}Fe_{ppt}$ (Eq. 2), assumes that Fe(III) precipitates directly after oxidation of $Fe(II)_{aq}$, which is likely not the case if the epsilon of the $\delta^{56}Fe_{aq}$ and $\delta^{56}Fe_{ppt}$ Rayleigh fits are different. Fits with an equilibrium model also resulted in unique slopes for the $\delta^{56}Fe_{aq}$ vs. the $\delta^{56}Fe_{ppt}$ data, and similar quality of fits (i.e., sum of chi^2) for each model for the $\delta^{56}Fe_{ppt}$ data (Table 2). Our isotopic data and fits suggest that the pool of Fe_{aq} is fractionated by a kinetic process during Fe(II) oxidation, whereas the $\delta^{56}Fe_{ppt}$ during Fe(III) precipitation could be controlled by kinetic or equilibrium fractionation, or a mixture of both models (Fig. 8). These observations imply the existence of a third phase of Fe, likely one of the components of $Fe(II/III)_{interm}$, which forms between Fe(II) oxidation and Fe(III) precipitation, in a multi-step fractionation process. Our data imply a ca. 1‰, fractionation from Fe_{aq} to the product of Fe(II) oxidation. However, without clear evidence of which Fe phase serves as an intermediate and in what capacity, it is not possible to rewrite Eq. (2) or define a fractionation factor or epsilon for the $\delta^{56}Fe_{ppt}$ data (Fig. 8).

In previous work with freshwater photoferrotroph cultures, the overall isotopic fractionation ($\varepsilon_{Fe_{ppt}-Fe_{aq}}$) was estimated to be 1.5 ± 0.2‰ from the difference between Fe_{ppt} and Fe_{aq} (i.e., $\Delta^{56}Fe_{ppt}-{}^{56}Fe_{aq}$) when the fraction of Fe(II) oxidized was less than 0.5 (Croal et al., 2004). The data from that study also did not clearly fit either a Rayleigh (kinetic) or equilibrium model (their Fig. 7). Experiments with cultures of the nitrate-reducing Fe(II)-oxidizing bacterium *Acidovorax* sp. BoFeN1, also at circumneutral pH. the $\Delta Fe(III)_{ppt}$–$Fe(II)_{aq}$ of 3‰, was related to a 2-step equilibrium-kinetic process (Kappler et al., 2010). These collected experiments characterizing Fe isotope fractionation by microbes oxidizing Fe(II) at circumneutral pH all noted that a single equilibrium or kinetic model could not explain the data, similar to what we observed.

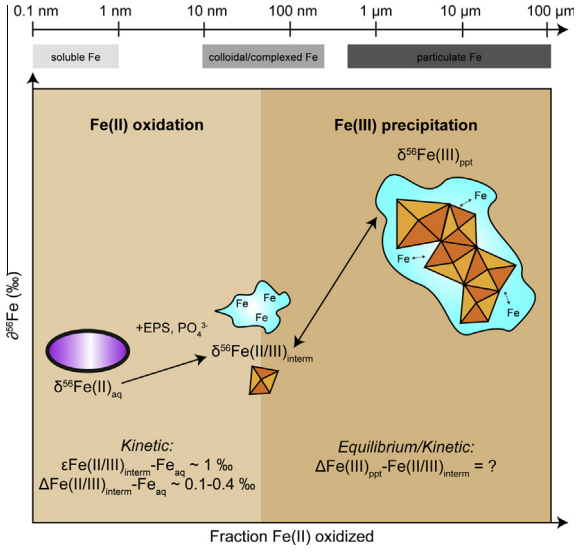

Fig. 8. Fe isotope fractionation during Fe(II) oxidation by *R. iodosum* is kinetically-controlled, forming soluble or colloidal Fe(II) and Fe(III) species ($Fe(II/III)_{interm}$) due to the presence of organic (e.g., EPS) and/or inorganic (e.g., PO_4^{3-}) ligands. Fe(III) minerals similar to ferrihydrite precipitate in isotopic equilibrium with $Fe(II/III)_{interm}$.

Croal et al. (2004) suggested either that an Fe(III)-organic ligand species may be in isotopic equilibrium with aqueous Fe(II) in their experiments with photoferrotrophs, or that precipitation of Fe(III) minerals caused a kinetic fractionation. However, they did not determine whether an Fe(III)-organic species was present in their experiments. There is previously reported microscopic evidence for an Fe(III)-organic ligand phase in cultures of *R. iodosum* during similar stages of Fe(II) oxidation (Wu et al., 2014), an observation that is relevant for the present study. Furthermore, we observed up to several hundred µM of $Fe(III)_{aq}$ present in both experiments where Fe_{aq} was separated from Fe_{ppt} by centrifugation (*Ri*-1 and *Ri*-2) and filtration (*Ri*-3; Fig. 1). Fe(III) was present in the aqueous phase despite the theoretical solubility of only sub-micromolar quantities of Fe(III) in seawater at pH 6.8 (Millero, 1998). Organic ligands can enhance the solubility of Fe(III) and produce a phase that is small enough to pass through a 0.22 µm filter (Bruland and Rue, 2001). Additionally, both Fe(II) and Fe(III) were detected in the H_2O and NaAc washes. An Fe(III)-organic ligand phase was spatially co-localized to Fe minerals in cultures of *R. iodosum*, suggesting a physical mechanism for precipitation of the mineral from Fe initially bound by an organic species (Wu et al., 2014). Due to the lighter isotopic composition of Fe_{ppt} with less stringent Fe separation protocols (i.e., *Ri*-1) and mass balance calculations (Eq. 4 and Supplementary Fig. 2), we suggest that $Fe(II/III)_{interm}$ may be isotopically lighter than Fe_{ppt}. In order to distinguish whether an organic phase may serve to stabilize Fe in an aqueous phase in cultures of *R. iodosum*, thereby influencing the pathway by which Fe(III) precipitates and is fractionated, it is necessary to determine the nature of the $Fe(II/III)_{interm}$ phase and the Fe precipitates formed during Fe(II) oxidation by *R. iodosum*.

4.2. Mineralogical transformations occurring during Fe(II) oxidation and Fe(III) precipitation

Although the predominant phases of Fe in our experiments are Fe_{aq} and Fe_{ppt}, 5–10% of the total Fe is present as the extractable $Fe(II/III)_{interm}$ phase throughout the course of experiments, in addition to the Fe(III) in the Fe_{aq} phase discussed above (Fig. 2 and Supplementary Table 1). In previous work, an Fe(III) phase was observed during Fe(II) oxidation by *R. iodosum* that was likely

soluble based on binding with a fluorescent sensor that does not bind to Fe(III) in minerals (Hao et al., 2013; Wu et al., 2014). This phase was co-localized to EPS, organics excreted by bacteria into their surroundings, based on the spatial overlap of fluorescence from a fluorescent Fe(III)-sensor and a fluorescent dye that binds EPS in confocal laser scanning microscopy (CLSM) images. The spatial overlap observed between Fe(III), EPS and the Fe minerals present (Wu et al., 2014) is similar to what is expected with co-precipitation of ferrihydrite and EPS (Mikutta et al., 2008). The existence of an Fe(III) phase bound to EPS could correspond to the $Fe(II/III)_{interm}$ we observed in H_2O and NaAc extractions of Fe_{ppt} and/or the soluble Fe(III) in $Fe_{aq.}$ If so, there are implications for the mineralogy and processes controlling isotope fractionation in biological and/or organic-rich Fe(II) oxidizing systems. We therefore used several complementary techniques to identify the nature of solid Fe phases present in our samples.

The parameters obtained by fitting the Mössbauer spectrum (Table 3) indicate that the Fe solid produced by *R. iodosum* during Fe(II) oxidation is a poorly crystalline Fe(III) phase. The sample is superparamagnetic at room temperature and starts to become magnetically ordered above 77 K, as indicated by the presence of a sextet in combination with a doublet (Fig. 4). The blocking temperature is defined as the temperature when the spectral areas of the doublet and sextet regions of a Mössbauer spectrum equal each other, thus as the spectral area of the doublet in the 77 K spectra is 28%, the sample must have a blocking temperature above 77 K. At 5 K the sample is fully magnetically ordered with center shift, quadrupole shift and hyperfine field values, which are indicative of ferrihydrite (van der Zee et al., 2003; Murad, 2010). Furthermore, the average surface area of $126 \pm 0.5\ m^2\ g^{-1}$ is consistent with the range of natural and synthetic ferrihydrite (Cornell and Schwertmann, 2003) All of these factors suggest that ferrihydrite is likely formed during Fe(II) oxidation by *R. iodosum*.

The fit of the EXAFS spectrum collected after all of the Fe(II) had been oxidized by *R. iodosum* (Fig. 5) utilized 2-line ferrihydrite, synthesized in the presence of Si, and a biogenic Fe(III) mineral sample collected from an Fe-rich mat likely inhabited by Fe(II)-oxidizing bacteria at a seafloor hydrothermal vent (Toner et al., 2009b). This seafloor sample had spectral features consistent with some of the bonds present in 2-line ferrihydrite and goethite, but was characterized by short-range ordering imposed by the predominance of edge-sharing octahedral linkages. In that work, it was suggested that organic carbon may play a role in truncating the polymerization of Fe(III)-minerals (Toner et al., 2009b). Similar short-range ordering can also arise from the presence of inorganic (i.e., SiO_4^{4-}, PO_4^{3-}) ligands during Fe(III) mineral precipitation (Voegelin et al., 2010; Swanner et al., 2011). In the case of *R. iodosum*, the medium contained no added Si, and much of the phosphate was removed during Fe(II) precipitation in our media preparation steps, resulting in ca. 40 μM PO_4^{3-} remaining in the medium at inoculation (Hohmann et al., 2010). However, EPS are excreted by *R. iodosum* during Fe(II) oxidation (Wu et al., 2014), perhaps leading to structural features similar to the biogenic Fe(III) mineral observed by Toner et al. (2009b). The dominant size fraction of particles is between 40 and 300 nm (Fig. 7), similar to the size range of colloidal, low-crystallinity, short-range order nanoparticles observed in cultures of microaerophillic Fe(II)-oxidizing bacteria (Swanner et al., 2011).

The PDF derived from the Fe solid formed by *R. iodosum* at the end of Fe(II) oxidation (Fig. 6) had similar spectral features to 2-line ferrihydrite (Michel et al., 2007b) and a Si-rich biogenic Fe(III)-mineral formed within an Fe(II)-oxidizing mat at a seafloor hydrothermal vent (Toner et al., 2012). The Fe–O bond in reference 2-line ferrihydrite is indicated by the peak at 1.97 Å (Michel et al., 2007b), and corresponds to the peak in the sample. In both the sample and the biogenic Fe(III) mineral, an additional peak was present at lower *r* distances due to association of an impurity. Slight offsets between Fe–Fe peaks in our sample and that of 2-line ferrihydrite (edge-sharing at 3.03 Å and corner-sharing 3.43 Å) are due to increased structural disorder, likely due to the presence of impurities (Cismasu et al., 2011; Toner et al., 2012), consistent with the attenuation of the PDF in our sample at higher *r*, and the small particle sizes (Fig. 7). For the solid sample, association of phosphate with ferrihydrite should have an impact on short-range ordering due to the formation of P–O–Fe bonds and/or phosphate polymers. Voegelin et al. (2010) noticed a decrease in edge-sharing Fe–Fe bonds based on EXAFS data in Fe(III) minerals with P:Fe of 0.12–1.2. Cell–Fe(III) mineral aggregates at the end of oxidation experiments by *R. iodosum* have P:Fe ratios of 0.04–0.05 as measured by ICP-MS. Although phosphate in the medium after filtration of initial Fe(II) precipitates should be low (40 μM) (Hohmann et al., 2010), it is possible that initial ferric precipitates during oxidation incorporate a higher amount of phosphate (Swanner et al., 2011), leading to the detection of the P–O bond and overall decrease in the structural order of produced minerals. As the sample was washed five times prior to analysis, it seems likely that any soluble or sorbed Fe(III) phases were removed during centrifugation and/or washing, although contributions of quantitatively minor Fe(III) phases (i.e., less than 5–10% of Fe) may not be detectable in the PDF.

4.3. The role of organics in biological Fe isotope fractionations

As organic matter and Fe remain in association in sediments on geological time scales (Lalonde et al., 2012), understanding the role of Fe-organics in Fe isotopic fractionation is critical to interpreting the biological history of Fe-rich marine sediments. We propose that the presence of Fe(III) in the Fe_{aq}, as well as the persistence of an $Fe(II/III)_{interm}$ phase during oxidation influences the isotopic compositions and evolution of the Fe_{aq} reservoir according to a kinetic process and the Fe_{ppt} reservoir through a separate kinetic and/or equilibrium process (Fig. 8). The Fe(III) in Fe_{aq} is likely to include an organic, ligand-type component, possibly EPS, based on the size fractions allowed through the filter (0.22 μm), and

previously published mineralogical and CLSM data during Fe(II) oxidation by *R. iodosum* (Wu et al., 2014). The $Fe(II/III)_{interm}$ phases may possibly also constitute Fe-organic phases, based on EXAFS results, or colloidal Fe phases formed as a result of impurities (e.g., PO_4^{3-}) inferred from X-ray total scattering data (Fig. 7). This conclusion is supported by the predominantly small size range of particles (99.7% < 1 μm) in the culture suspensions (Fig. 8). The $\delta^{56}Fe(II/III)_{interm}$ calculated with Eq. (4) from DS measurements of *Ri*-3 was 0.1–0.4‰ heavier than the Fe_{aq} (Supplementary Fig. 2). The kinetic fit of Fe_{aq} suggests rather a fractionation close to 1‰ between the immediate product of Fe(II) oxidation and Fe_{aq} (Fig. 3 and Table 2). This disagreement could stem from the errors in our Fe concentration determination propagating through Eq. (4), or from the effect of multiple Fe phases with distinct Fe isotope compositions within $Fe(II/III)_{interm}$ and multiple fractionation processes between Fe(II) oxidation and Fe(III) precipitation (Fig. 8). The persistent fraction of total Fe potentially bound to an organic phase could impose a kinetic fractionation associated with binding of Fe(III) to an organic phase with high Fe affinity (Brantley et al., 2001), consistent with the interpretation that the Fe_{aq} pool is fractionated by a kinetically-controlled process during Fe(II) oxidation (Fig. 8). Strong organic Fe ligands can discriminate toward the lighter isotope (Brantley et al., 2001), However, discrimination of ligands for the light isotopes was observed when Fe(II) was mobilized and oxidized out of a mixed-valence Fe mineral (hornblende; Brantley et al., 2001). When Fe was mobilized by organic ligands from a pool of Fe(III) (in goethite), there was no fractionation (Brantley et al., 2004). And, experiments with the synthetic siderophore desferrioxamine B discriminated for heavier isotopes of Fe(III) from a dissolved inorganic Fe(III) pool with a fractionation factor of 0.6‰ (Dideriksen et al., 2008). Heavier Fe was also enriched in colloidal oxic river particles that contained abundant organic C (Ilina et al., 2013). These results collectively suggest that organic ligands may fractionate Fe isotopes, with the direction and magnitude of fractionation dependent on the identity of the ligand and the oxidation state of Fe.

The evolution of $\delta^{56}Fe_{ppt}$ appears to be controlled by a precipitation process that is distinct from the fate of Fe(III) during from Fe(II) oxidation. The data are consistent with both kinetic and equilibrium fractionation models (Fig. 3 and Table 2). We did not evaluate the possibility of a Rayleigh fit of the $\delta^{56}Fe_{ppt}$ data where Eq. (2) was modified to account for Fe_{ppt} forming from $Fe(II/III)_{interm}$ rather than Fe_{aq}. As there may be multiple fractions of Fe within $Fe(II/III)_{interm}$ with different $\delta^{56}Fe$, which we did not measure, and Fe_{ppt} could form from one or more of these fractions, further definition of these phases and their composition would be necessary to rewrite Eq. (2). Nevertheless, equilibrium fractionation was previously proposed to explain $\delta^{56}Fe_{ppt}$ trends during similar experiments with nitrate-dependent Fe(II) oxidizing microbes at neutral pH (Kappler et al., 2010). Equilibrium exchange of Fe_{ppt} may be promoted in a system with nm-scale Fe(III) minerals with high surface areas (Kappler et al., 2010). The short-range ordered ferrihydrite mineral that forms during Fe(II) oxidation by *R. iodosum* may therefore be suited to attainment of isotopic equilibrium with other Fe phases such as $Fe(II/III)_{interm}$ (Fig. 8). Furthermore, if precipitation is slow, such as if Fe(III) precipitates from an organic-ligand bound phase or transforms from a colloidal phase, equilibrium isotope exchange could be supported (Johnson et al., 2002; Anbar et al., 2005; Balci et al., 2006).

4.4. Toward an Fe isotope biosignature for microbial Fe(II) oxidation?

This slight discrimination for the heavier isotope during Fe(II) oxidation and formation of the $Fe(II/III)_{interm}$ phase we infer from our data is in the same direction as Fe(III) mineral precipitation, but unlike the expected favoring of light isotopes by biological processing. It was once hoped that a unique, biological fractionation signature existed for biological Fe redox systems (Beard et al., 1999), but during microbial Fe(II) oxidation the overall fractionation seems to be dominated by precipitates favoring the heavy isotope. If isotopically distinct Fe-organic phases and/or colloidal minerals are intermediates or stabilized during certain types of biological oxidation, the existence of such phases has implications for interpreting the biological contribution to Fe(II) oxidation in both modern and ancient systems.

In several modern, circumneutral Fe(II)-oxidizing systems, there exist pools of Fe_{ppt} that are lighter than expected if precipitation of Fe(III) minerals was the dominant process causing fractionation from the $Fe(II)_{aq}$ pool. For instance, at Chocolate Pots Hot Springs in Yellowstone NP, the degree of fractionation between aqueous Fe(II) and Fe(III) minerals is less than expected given the extent of Fe(II) oxidation (Wu et al., 2013). In other words, the Fe_{ppt} is lighter than it should be using published fractionation factors. Those authors suggest that the high Si concentrations (up to 150 ppm) at that spring promote the formation of an Fe-Si species that sorbs to the Fe(III) mineral surface. Based on their previous experimental work, such an isotopically light phase was detected in 5 N HCl extractions, and suggested to be a sorbing Fe–Si species (Wu et al., 2012). At Chocolate Pots, the microbial community is dominated by cyanobacteria that form extensive, organic-rich mats (Pierson et al., 1999). An additional possibility is that the isotopically light phase (relative to Fe_{aq}) inferred for Chocolate Pots could be Fe bound to organic ligands, or present in a short-range ordered colloid mineral phase generated as a result of Si impurities (e.g., Toner et al., 2012), similar to the $Fe(II/III)_{interm}$ phase we report on here.

Chocolate Pots hot spring is not the only environment where the isotopic composition of Fe-rich mats is lighter than expected for a single, kinetically-controlled fractionation process. In hydrothermally-precipitated sediments of the Jan Mayen hydrothermal field, Fe_{ppt} had an isotopic composition similar to the fluids, or occasionally slightly heavier (Moeller et al., 2014). In this work, the authors invoke partial oxidation of $Fe(II)_{aq}$ as a mechanism for this lighter than expected composition, or alternately the input of a secondary source of light Fe leached from underlying

basalt (cf. Rouxel et al., 2003), or microbial Fe(III) reduction providing an additional source of isotopically depleted $Fe(II)_{aq}$ within the hosting sediments. A further possibility is that Fe binds to organic phases within the mat and/or precipitates in the presence of Si, generating colloidal Fe phases with an isotopic composition only slightly heavier than the hydrothermal $Fe(II)_{aq}$ source. In a series of spectroscopic investigations of mats and particles from hydrothermal systems, Toner et al. (2009b, 2012) found evidence for the presence of Fe-binding organic ligands and Si in promoting the formation of short-range ordered (poorly crystalline and low polymerization) Fe oxides in a biogenic Fe mat from Loihi seamount. A follow-up study noted the persistence of Fe(II) associated with organic material in hydrothermal plumes (Toner et al., 2009a), suggesting a mechanism for transporting Fe(II) (i.e., partial oxidation) even in oxic systems. Between stabilizing Fe(II) in solution and producing an only slightly heavier Fe(III) pool, organic phases (and Si) may contribute to the lower than expected overall fractionations observed in natural and biological Fe(II)-oxidizing systems. If this is the case, it might be expected that Fe associated with organic stalks of mFeOB shows a similar small fractionation from the $Fe(II)_{aq}$ source as we see in our experiments. To our knowledge, such a measurement has not been made but would be a test of this hypothesis. Further work to isolate and isotopically analyze soluble Fe-organic phases would also be of value.

Shifting our gaze to the ancient, our results may yet offer implications for the interpretation of biological involvement in Precambrian IF deposition. Oxidized Fe minerals in IF tend to be isotopically heavy, while mixed-valence phases are isotopically light (Johnson et al., 2005, 2008). It has been suggested that isotopically light Fe in IF results from the fractionation imposed by microbial Fe(III) reduction, which produces isotopically lighter $Fe(II)_{aq}$. Certainly Fe(III) reduction via reaction with organic matter was involved in forming Fe(II) phases such as siderite in Precambrian IF, which bear isotopically light carbon that does not reflect precipitation in equilibrium with a seawater carbonate source (Johnson et al., 2013). Yet abiotic reactions between organic carbon and Fe(III) minerals at elevated temperature and pressure can also generate mixed-valence Fe minerals including siderite and magnetite (Posth et al., 2013a), the Fe isotope composition of which is currently unknown, but likely to be retained through low-temperature metamorphism (Frost et al., 2007). Another unconstrained variable is the role of the intimate association of Fe with organic carbon that is observed in modern sediments and biologically-precipitated Fe(III) mats (Toner et al., 2009b; Lalonde et al., 2012) in preserving primary Fe(III) minerals such as ferrihydrite. Toner et al. (2012) observed that a short-range ordered ferrihydrite associated with Si and biogenic material did not transform to hematite until 400℃, as opposed to ready transformation of more ordered synthetic ferrihydrite to hematite at much lower temperatures (Cornell and Schwertmann, 2003; Posth et al., 2013a). These experiments indicate that biogenic and/or colloidal Fe(III)-oxides with impurities may be more resistant to thermal reduction. Low-temperature microbial Fe(III) reduction may also be limited in these primary Fe(III) oxide deposits, such as those near seafloor hydrothermal systems, because the organic carbon content may be too low to support their respiration, or because organic material such as mFeOB stalks is coated with Fe, preventing reduction (Emerson, 2009). Therefore, biologically-precipitated Fe(III) minerals such as those produced by photoferrotrophs or mFeOB might be expected to be preserved in the IF record as dominantly Fe(III) phases, in which Fe could be isotopically lighter than expected using fractionation factors determined for abiotic Fe(II) oxidation.

5. CONCLUSIONS

The patterns of Fe isotope fractionation between Fe_{aq} and Fe_{ppt} during Fe(II) oxidation by the photoferrotroph *R. iodosum* are highly influenced by soluble Fe(III) phases, inferred to be organically bound, and intermediate/sorbed phases of Fe(II) and Fe(III) that can be removed from the $Fe(III)_{ppt}$ by water and NaAc washes. Based on bulk chemistry, mineralogical, and microscopic inferences, it is likely that these soluble or intermediate phases consist of both Fe(II) and Fe(III), bound to an organic phase or forming colloidal, low crystallinity Fe minerals. These intermediate phases may be slightly isotopically heavier than the Fe_{aq}, but lighter than Fe_{ppt}. The occurrence of such intermediate phases is consistent with kinetic isotope fractionation during binding of either Fe(II) or Fe(III) to strong organic ligands, or Fe precipitation in the presence of Si or other ligands that interfere with Fe(III) mineral growth (e.g., phosphate). Formation of Fe_{ppt} may occur from these phases in a kinetic or equilibrium fractionation process. Our evidence for such isotopically distinct Fe-organic or colloidal phases during microbially-influenced Fe(II) oxidation will be useful in unraveling the contribution of organics to the Fe isotope signatures of other Fe-rich, biological systems, and hints that Fe isotope signatures from organic-rich systems during Earth's past may indicate an active biological community. However, it is not clear whether such a signature is unique to photoferrotrophic organisms, and it could rather signify a general biological contribution to Fe(II) oxidation.

ACKNOWLEDGEMENTS

We thank Ellen Struve for performing Mastersizer and BET analyses. Stefan Lalonde carried out ICP-MS analysis. Portions of this research were carried out at the Stanford Synchrotron Radiation Lightsource (SSRL), a directorate of SLAC National Accelerator Laboratory and an Office of Science User Facility operated by the U.S. Department of Energy Office of Science by Stanford University. We thank Ryan Davis for assistance in EXAFS measurements, Brandy Toner for use of her EXAFS spectra, and Graham Lau for validating the mineralogy of Fe EXAFS standards with XRD. The use of the Advanced Photon Source, an Office of Science User Facility operated for the U.S. Department of Energy (DOE) Office of Science by Argonne National Laboratory, was supported by the U.S. DOE under Contract No. DE-AC02-06CH11357. We thank Karina Chapman, Peter Chupas, and Kevin Beyer for their support at APS beamline 11-ID-B. EDS was supported by a National Science Foundation (NSF) International Research Fellowship

(No. 1064391). W.W. received support from CAS/SAFEA International Partnership Program for Creative Research Teams (KZCX2-YW-T10) and NSFC (No. 40821091). A.K. was supported by the German Research Foundation (DFG, KA 1736/24-1), and by the European Research Council under the European Union's Seventh Framework Programme (FP/2007–2013)/ERC Grant, Agreement n. 307320 – MICROFOX.

APPENDIX A. SUPPLEMENTARY DATA

Supplementary data associated with this article can be found, in the online version, at http://dx.doi.org/10.1016/j.gca.2015.05.024.

REFERENCES

Anbar A. D., Jarzecki A. A. and Spiro T. G. (2005) Theoretical investigation of iron isotope fractionation between $Fe(H_2O)_6^{3+}$ and $Fe(H_2O)_6^{2+}$: implications for iron stable isotope geochemistry. *Geochim. Cosmochim. Acta* **69**, 825–837.

Balci N., Bullen T. D., Witte-Lien K., Shanks W. C., Motelica M. and Mandernack K. W. (2006) Iron isotope fractionation during microbially stimulated Fe(II) oxidation and Fe(III) precipitation. *Geochim. Cosmochim. Acta* **70**, 622–639.

Beard B. L., Johnson C. M., Cox L., Sun H., Nealson K. and Aguilar C. (1999) Iron isotope biosignatures. *Science* **285**, 1889–1892.

Beukes N. J. and Klein C. (1992) Models for iron-formation deposition. In *The Proterozoic Biosphere: A Multidisciplinary Study* (eds. J. W. Schopf and C. Klein). Cambridge University Press, New York, pp. 147–151.

Brantley S. L., Liermann L. J. and Bullen T. D. (2001) Fractionation of Fe isotopes by soil microbes and organic acids. *Geology* **29**, 535–538.

Brantley S. L., Liermann L. J., Guyunn R. L., Anbar A., Icopini G. A. and Barling J. (2004) Fe isotopic fractionation during mineral dissolution with and without bacteria. *Geochim. Cosmochim. Acta* **68**, 3189–3204.

Bruland K. W. and Rue E. L. (2001) Iron: analytical methods for the determination of concentrations and speciation. In *The Biogeochemistry of Iron in Seawater* (eds. K. A. Hunter and D. R. Turner). John Wiley and Sons, 255, p. 289.

Bullen T. D., White A. F., Childs C. W., Vivit D. V. and Schulz M. S. (2001) Demonstration of significant abiotic iron isotope fractionation in nature. *Geology* **29**, 699–702.

Canfield D. E. and Farquhar J. (2009) Animal evolution, bioturbation, and the sulfate concentration of the oceans. *Proc. Natl. Acad. Sci. USA* **106**, 8123–8127.

Chan C. S., De Stasio G., Welch S. A., Girasole M., Frazer B. H., Nesterova M. V., Fakra S. C. and Banfield J. F. (2004) Microbial polysaccharides template assembly of nanocrystal fibers. *Science* **303**, 1656–1658.

Chan C. S., Fakra S. C., Edwards D. C., Emerson D. and Banfield J. F. (2009) Iron oxyhydroxide mineralization on microbial extracellular polysaccharides. *Geochim. Cosmochim. Acta* **73**, 3807–3818.

Chan C. S., Fakra S. C., Emerson D., Fleming E. J. and Edwards K. J. (2011) Lithotrophic iron-oxidizing bacteria produce organic stalks to control mineral growth: implications for biosignature formation. *ISME J.* **5**, 717–727.

Cismasu A. C., Michel F. M., Tcaciuc A. P., Tyliszczak T. and Brown J. G. E. (2011) Composition and structural aspects of naturally occurring ferrihydrite. *C.R. Geosci.* **343**, 210–218.

Cloud P. E. (1965) Significance of gunflint (Precambrian) microflora. *Science* **148**, 27–35.

Cornell R. M. and Schwertmann U. (2003) *The Iron Oxides – Structure, Properties, Reactions, Occurence and Uses*. Wiley VCH Publishing Group, Weinheim, Germany.

Croal L. R., Johnson C. M., Beard B. L. and Newman D. K. (2004) Iron isotope fractionation by Fe(II)-oxidizing photoautotrophic bacteria. *Geochim. Cosmochim. Acta* **68**, 1227–1242.

Croal L. R., Jiao Y., Kappler A. and Newman D. K. (2009) Phototrophic Fe(II) oxidation in an atmosphere of H_2: implications for Archean banded iron formations. *Geobiology* **7**, 21–24.

Crosby H. A., Roden E. E., Johnson C. M. and Beard B. L. (2007) The mechanisms of iron isotope fractionation produced during dissimilatory Fe (III) reduction by *Shewanella putrefaciens* and *Geobacter sulfurreducens*. *Geobiology* **5**, 169–189.

Crowe S. A., Jones C., Katsev S., Magen C. d., O'Neill A. H., Sturm A., Canfield D. E., Haffner G. D., Mucci A., Sundby B. and Fowle D. A. (2008) Photoferrotrophs thrive in an Archean Ocean analogue. *Proc. Natl. Acad. Sci. USA* **105**, 15938–15943.

Dideriksen K., Baker J. A. and Stipp S. L. S. (2008) Equilibrium Fe isotope fractionation between inorganic aqueous Fe(III) and the siderophore complex, Fe(III)-desferrioxamine B. *Earth Planet. Sci. Lett.* **269**, 280–290.

Eickhoff M., Birgel D., Talbot H. M., Peckmann J. and Kappler A. (2013) Oxidation of Fe(II) leads to increased C-2 methylation of pentacyclic triterpenoids in the anoxygenic phototrophic bacterium *Rhodopseudomonas palustris* strain TIE-1. *Geobiology* **11**, 268–278.

Emerson D. (2009) Potential for Iron-reduction and iron-cycling in iron oxyhydroxide-rich microbial mats at Loihi Seamount. *Geomicrobiol. J.* **26**, 639–647.

Frost C., von Blanckenburg F., Schoenberg R., Frost B. and Swapp S. (2007) Preservation of Fe isotope heterogeneities during diagenesis and metamorphism of banded iron formation. *Contrib. Miner. Petrol.* **153**, 211–235.

Hammersley A. P. (1998) *Fit2D v9.129 Reference Manual V. 31*. European Synchrotron Radiation Facility, Grenoble, France, p. 306.

Hao L., Li J., Kappler A. and Obst M. (2013) Mapping of heavy metal ion sorption to cell-extracellular polymeric substance-mineral aggregates by using metal-selective fluorescent probes and confocal laser scanning microscopy. *Appl. Environ. Microbiol.* **79**, 6524–6534.

Hegler F., Schmidt C., Schwarz H. and Kappler A. (2010) Does a low-pH microenvironment around phototrophic FeII-oxidizing bacteria prevent cell encrustation by FeIII minerals?. *FEMS Microbiol. Ecol.* **74** 592–600.

Hohmann C., Winkler E., Morin G. and Kappler A. (2010) Anaerobic Fe(II)-oxidizing bacteria show As resistance and co-precipitate As during Fe(III) mineral precipitation. *Environ. Sci. Technol.* **44**, 94–101.

Ilina S. M., Poitrasson F., Lapitskiy S. A., Alekhin Y. V., Viers J. and Pokrovsky O. S. (2013) Extreme iron isotope fractionation between colloids and particles of boreal and temperate organic-rich waters. *Geochim. Cosmochim. Acta* **101**, 96–111.

John S. G., Mendez J., Moffett J. and Adkins J. (2012) The flux of iron and iron isotopes from San Pedro Basin sediments. *Geochim. Cosmochim. Acta* **93**, 14–29.

Johnson C. M., Skulan J. L., Beard B. L., Sun H., Nealson K. H. and Braterman P. S. (2002) Isotopic fractionation between Fe(III) and Fe(II) in aqueous solutions. *Earth Planet. Sci. Lett.* **195**, 141–153.

Johnson C. M., Roden E. E., Welch S. A. and Beard B. L. (2005) Experimental constraints on Fe isotope fractionation during magnetite and Fe carbonate formation coupled to dissimilatory

hydrous ferric oxide reduction. *Geochim. Cosmochim. Acta* **69**, 963–993.

Johnson C. M., Beard B. L., Klein C., Beukes N. J. and Roden E. E. (2008) Iron isotopes constrain biologic and abiologic processes in banded iron formation genesis. *Geochim. Cosmochim. Acta* **72**, 151–169.

Johnson C. M., Ludois J. M., Beard B. L., Beukes N. J. and Heimann A. (2013) Iron formation carbonates: paleoceanographic proxy or recorder of microbial diagenesis? *Geology* **41**, 1147–1150.

Kappler A. and Newman D. K. (2004) Formation of Fe(III)-minerals by Fe(II)-oxidizing photoautotrophic bacteria. *Geochim. Cosmochim. Acta* **68**, 1217–1226.

Kappler A., Pasquero C., Konhauser K. O. and Newman D. K. (2005) Deposition of banded iron formations by anoxygenic phototrophic Fe(II)-oxidizing bacteria. *Geology* **33**, 865–868.

Kappler A., Johnson C. M., Crosby H. A., Beard B. L. and Newman D. K. (2010) Evidence for equilibrium iron isotope fractionation by nitrate-reducing iron(II)-oxidizing bacteria. *Geochim. Cosmochim. Acta* **74**, 2826–2842.

Kempe S. and Degens E. T. (1985) An early soda ocean? *Chem. Geol.* **53**, 95–108.

Konhauser K. O., Newman D. K. and Kappler A. (2005) The potential significance of microbial Fe(III) reduction during deposition of Precambrian banded iron formations. *Geobiology* **3**, 167–177.

Konhauser K. O., Amskold L., Lalonde S. V., Posth N. R., Kappler A. and Anbar A. D. (2007a) Decoupling photochemical Fe(II) oxidation from shallow-water BIF deposition. *Earth Planet. Sci. Lett.* **258**, 87–100.

Konhauser K. O., Lalonde S. V., Amskold L. and Holland H. D. (2007b) Was there really an archean phosphate crisis? *Science* **315**, 1234.

Krepski S. T., Emerson D., Hredzak-Showalter P. L., Luther, III, G. W. and Chan C. S. (2013) Morphology of biogenic iron oxides records microbial physiology and environmental conditions: toward interpreting iron microfossils. *Geobiology* **5**, 457–471.

Lalonde K., Mucci A., Ouellet A. and Gélinas Y. (2012) Preservation of organic matter in sediments promoted by iron. *Nature* **483**, 198–200.

Michel F. M., Ehm L., Antao S. M., Lee P. L., Chupas P. J., Liu G., Strongin D. R., Schoonen M. A. A., Phillips B. L. and Parise J. B. (2007a) The structure of ferrihydrite, a nanocrystalline material. *Science* **316**, 1726–1729.

Michel F. M., Ehm L., Liu G., Han W. Q., Antao S. M., Chupas P. J., Lee P. L., Knorr K., Eulert H., Kim J., Grey C. P., Celestian A. J., Gillow J. B., Schoonen M. A. A., Strongin D. R. and Parise J. B. (2007b) Similarities in 2- and 6-line ferrihydrite based on pair distribution function analysis of X-ray total scattering. *Chem. Mater.* **19**, 1489–1496.

Michel F. M., Barrón V., Torrent J., Morales M. P., Serna C. J., Boily J.-F., Liu Q., Ambrosini A., Cismasu A. C. and Brown G. E. (2010) Ordered ferrimagnetic form of ferrihydrite reveals links among structure, composition, and magnetism. *Proc. Natl. Acad. Sci. USA* **107**, 2787–2792.

Mikutta C., Mikutta R., Bonneville S., Wagner F., Voegelin A., Christl I. and Kretzschmar R. (2008) Synthetic coprecipitates of exopolysaccharides and ferrihydrite. Part I: characterization. *Geochim. Cosmochim. Acta* **72**, 1111–1127.

Millero F. J. (1998) Solubility of Fe(III) in seawater. *Earth Planet. Sci. Lett.* **154**, 323–329.

Miot J., Benzerara K., Obst M., Kappler A., Hegler F., Schädler S., Bouchez C., Guyot F. and Morin G. (2009) Extracellular iron biomineralization by photoautotrophic iron-oxidizing bacteria. *Appl. Environ. Microbiol.* **75**, 5586–5591.

Moeller K., Schoenberg R., Grenne T., Thorseth I. H., Drost K. and Pedersen R. B. (2014) Comparison of iron isotope variations in modern and Ordovician siliceous Fe oxyhydroxide deposits. *Geochim. Cosmochim. Acta* **126**, 422–440.

Murad E. (2010) Mössbauer spectroscopy of clays, soils and their mineral constituents. *Clay Miner.* **45**, 413–430.

Pierson B. K., Paranteau M. N. and Griffin B. M. (1999) Phototrophs in high-iron-concentration microbial mats: physiological ecology of phototrophs in an iron-depositing hot spring. *Appl. Environ. Microbiol.* **65**, 5474–5483.

Planavsky N., Rouxel O., Bekker A., Shapiro R., Fralick P. and Knudsen A. (2009) Iron-oxidizing microbial ecosystems thrived in late Paleoproterozoic redox-stratified oceans. *Earth Planet. Sci. Lett.* **286**, 230–242.

Porsch K. and Kappler A. (2011) FeII oxidation by molecular O_2 during HCl extraction. *Environ. Chem.* **8**, 190–197.

Posth N. R., Köhler I., D. Swanner E., Schröder C., Wellmann E., Binder B., Konhauser K. O., Neumann U., Berthold C., Nowak M. and Kappler A. (2013a) Simulating Precambrian banded iron formation diagenesis. *Chem. Geol.* **362**.

Posth N. R., Konhauser K. O. and Kappler A. (2013b) Microbiological processes in banded iron formation deposition. *Sedimentology* **60**, 1733–1754.

Qiu X., Thompson J. W. and Billinge S. J. L. (2004) PDFgetX2: a GUI-driven program to obtain the pair distribution function from X-ray powder diffraction data. *J. Appl. Crystallogr.* **37**, 678.

Rancourt D. G. and Ping J. Y. (1991) Voigt-based methods for arbitrary-shape static hyperfine parameter distributions in Mössbauer spectroscopy. *Nucl. Instrum. Methods Phys. Res., Sect. B* **58**, 85–97.

Rouxel O., Dobbek N., Ludden J. and Fouquet Y. (2003) Iron isotope fractionation during oceanic crust alteration. *Chem. Geol.* **202**, 155–182.

Saini G. and Chan C. S. (2012) Near-neutral surface charge and hydrophilicity prevent mineral encrustation of Fe-oxidizing micro-organisms. *Geobiology* **11**(2), 191–200.

Schaedler S., Burkhardt C., Hegler F., Straub K. L., Miot J., Benzerara K. and Kappler A. (2009) Formation of cell–iron–mineral aggregates by phototrophic and nitrate-reducing anaerobic Fe(II)-oxidizing bacteria. *Geomicrobiol. J.* **26**, 93–103.

Schmid G., Zeitvogel F., Hao L., Ingino P., Floetenmeyer M., Stierhof Y.-D., Schroeppel B., Burkhardt C., Kappler A. and Obst M. (2014) 3D analysis of bacterial cell–(iron)mineral aggregates formed during Fe(II) oxidation by the nitrate-reducing *Acidovorax* sp. strain BoFeN1 using complementary microscopy tomography approaches. *Geobiology* **12**, 340–361.

Schoenberg R. and Von Blanckenburg F. (2005) An assessment of the accuracy of stable Fe isotope ratio measurements on samples with organic and inorganic matrices by high-resolution multicollector ICP-MS. *Int. J. Mass Spectrom.* **242**, 257–272.

Schwertmann U. and Cornell R. M. (2000) *Iron Oxides in the Laboratory*, 2nd ed. Wiley-VCH Verlag GmbH, Weinheim.

Shannon R. D. (1976) Revised effective ionic radii and systematic studies of interatomic distances in halides and chalcogenides. *Acta Crystallogr. A* **32**, 751–767.

Staubwasser M., Schoenberg R., von Blanckenburg F., Kruger S. and Pohl C. (2013) Isotope fractionation between dissolved and suspended particulate Fe in the oxic and anoxic water column of the Baltic Sea. *Biogeosciences* **10**, 233–245.

Straub K. L., Rainey F. R. and Widdel F. (1999) Rhodovulum iodosum sp. nov. and Rhodovulum robiginosum sp. nov., two new marine phototrophic ferrous-iron-oxidizing purple bacteria. *Int. J. Syst. Bacteriol.* **49**, 729–735.

Stookey L. L. (1970) Ferrozine - a new spectrophotometric reagent for iron. *Anal. Chem.* **42**(7), 779–781.

Swanner E. D., Nell R. M. and Templeton A. S. (2011) *Ralstonia* species mediate Fe-oxidation in circumneutral, metal-rich subsurface fluids of Henderson mine, CO. *Chem. Geol.* **284**, 339–350.

Toner B. M., Fakra S. C., Manganini S. J., Santelli C. M., Marcus M. A., Moffett J. W., Rouxel O., German C. R. and Edwards K. J. (2009a) Preservation of iron(II) by carbon-rich matrices in a hydrothermal plume. *Nat. Geosci.* **2**, 197–201.

Toner B. M., Santelli C. M., Marcus M. A., Wirth R., Chan C. S., McCollom T., Bach W. and Edwards K. J. (2009b) Biogenic iron oxyhydroxide formation at mid-ocean ridge hydrothermal vents: Juan de Fuca Ridge. *Geochim. Cosmochim. Acta* **73**, 388–403.

Toner B. M., Berquó T. S., Michel F. M., Sorensen J. V., Templeton A. S. and Edwards K. J. (2012) Mineralogy of iron microbial mats from Loihi Seamount. *Front. Microbiol.* **3**.

van der Zee C., Roberts D. R., Rancourt D. G. and Slomp C. P. (2003) Nanogoethite is the dominant reactive oxyhydroxide phase in lake and marine sediments. *Geology* **31**, 993–996.

Voegelin A., Kaegi R., Frommer J., Vantelon D. and Hug S. J. (2010) Effect of phosphate, silicate, and Ca on Fe(III)-precipitates formed in aerated Fe(II)- and As(III)-containing water studied by X-ray absorption spectroscopy. *Geochim. Cosmochim. Acta* **74**, 164–186.

Webb S. M. (2005) SIXpack: a graphical user interface for XAS analysis using IFEFFIT. *Phys. Scr.* **2005**, 1011.

Welch S. A., Beard B. L., Johnson C. M. and Braterman P. S. (2003) Kinetic and equilibrium Fe isotope fractionation between aqueous Fe(II) and Fe(III). *Geochim. Cosmochim. Acta* **67**, 4231–4250.

Wilson J. P., Fischer W. W., Johnston D. T., Knoll A. H., Grotzinger J. P., Walter M. R., McNaughton N. J., Simon M., Abelson J., Schrag D. P., Summons R., Allwood A., Andres M., Gammon C., Garvin J., Rashby S., Schweizer M. and Watters W. A. (2010) Geobiology of the late Paleoproterozoic Duck Creek Formation, Western Australia. *Precambr. Res.* **179**, 135–149.

Wu L., Percak-Dennett E. M., Beard B. L., Roden E. E. and Johnson C. M. (2012) Stable iron isotope fractionation between aqueous Fe(II) and model Archean ocean Fe-Si coprecipitates and implications for iron isotope variations in the ancient rock record. *Geochim. Cosmochim. Acta* **84**, 14–28.

Wu L., Brucker R. P., Beard B. L., Roden E. E. and Johnson C. M. (2013) Iron isotope characteristics of hot springs at Chocolate Pots, Yellowstone National Park. *Astrobiology* **13**, 1091–1101.

Wu W., Swanner E. D., Hao L., Zeitvogel F., Obst M., Pan Y. and Kappler A. (2014) Characterization of the physiology and cell–mineral interactions of the marine anoxygenic phototrophic Fe(II)-oxidizer *Rhodovulum iodosum* – implications for Precambrian Fe(II) oxidation. *FEMS Microbiol. Ecol.* **88**, 503–515.

Associate editor: Andrew Ross Bowie